REVIEWS

Alloys

ADVANCED
ENGINEERING
MATERIALS

www.aem-journal.com

High-Entropy Alloys: Potential Candidates for High-Temperature Applications – An Overview

Sathiyamoorthi Praveen and Hyoung Seop Kim*

Multi-principal elemental alloys, commonly referred to as high-entropy alloys (HEAs), are a new class of emerging advanced materials with novel alloy design concept. Unlike the design of conventional alloys, which is based on one or at most two principal elements, the design of HEA is based on multi-principal elements in equal or near-equal atomic ratio. The advent of HEA has revived the alloy design perception and paved the way to produce an ample number of compositions with different combinations of promising properties for a variety of structural applications. Among the properties possessed by HEAs, sluggish diffusion and strength retention at elevated temperature have caught wide attention. The need to develop new materials for high-temperature applications with superior high-temperature properties over superalloys has been one of the prime concerns of the high-temperature materials research community. The current article shows that HEAs have the potential to replace Ni-base superalloys as the next generation high-temperature materials. This review focuses on the phase stability, microstructural stability, and high-temperature mechanical properties of HEAs. This article will be highly beneficial for materials science and engineering community whose interest is in the development and understanding of HEAs for high-temperature applications.

1. Introduction

Alloying is defined as the addition of a minor quantity of one or more elements to primary metal to achieve promising changes in mechanical, physical, and chemical properties.[1] Fascinatingly, the alloying technique that plays a significant role in physical metallurgy process was an accidental discovery.[2] Bronze, an alloy of Cu and Sn, was the first alloy to be discovered by humankind in ≈3000 BC.[3] Since the accidental discovery of bronze, the alloy development strategies have been fixated around one or at most two principal elements until the recent discovery of high-entropy alloys (HEAs) in 2004.[2,4–6] Astonishingly, it took many decades to develop an alloy based on multi-principal elements. Before the discovery of HEAs, the design of alloys with multi-principal elements was expected to form complex microstructures based on the understanding of classical physical metallurgy principles.[2,7] Furthermore, intermediate phase/compounds are widely observed in the middle of most of the binary phase diagrams.[8] As a result, the alloy design has been limited to one or two principal elements to prevent the formation of complex microstructure, which may be difficult to process, analyze, and can adversely affect the mechanical properties. In contrast, Yeh et al. and Cantor et al.'s independent research works on multi-principal elemental alloys demonstrated the formation of simple microstructures with enhanced properties.[4,9–11] This novel discovery has changed the perception of alloy design based on multi-principal elements. Yeh et al. postulated a theory based on the configurational entropy for the formation of simple microstructure rather than the anticipated complex phase and compounds formation. They proposed that the increase in configurational entropy due to an increase in the number of elements would reduce the free energy of the alloy system, which in turn would stabilize the solid solution.[4,12–14] Since then, these multi-principal elemental alloys have been widely referred to as high-entropy alloys.

However, the hypothesis based solely on the configurational entropy for the formation of solid solution has been a debatable topic in this field.[15–22] In several studies, the formation of compounds and secondary phases have been observed,[15,19,23–25] which implies that configurational entropy alone is not sufficient to suppress the compound formation. Moreover, single phase HEAs were observed only in a particular compositional range, and phase separation was observed in most of the HEAs.[21,26–32] The thermodynamic analysis of multicomponent alloys implies that enthalpy and non-configurational entropy play significant roles in phase stability, and the configurational entropy plays a primary role only when a single phase is observed.[15] Moreover, the formation of the random solid solution depends on various factors such as alloy melting temperature, processing temperature, interatomic correlations, and the characteristics of

Dr. H. S. Kim, Dr. S. Praveen
Center for High Entropy Alloys
Pohang University of Science and Technology (POSTECH),
Pohang 37673, Republic of Korea
E-mail: hskim@postech.ac.kr

Dr. H. S. Kim
Department of Mater. Sci. Eng.
Pohang University of Science and Technology (POSTECH),
Pohang 37673, Republic of Korea

Dr. Praveen Sathiyamoorthi is currently a Korea Research Fellow in the Department of Materials Science and Engineering at Pohang University of Science and Technology, South Korea. He received his Ph.D. (2016) in Metallurgical and Materials Engineering from Indian Institute of Technology Madras, India. His current research interest includes high entropy alloys, high-temperature deformation behavior, high-pressure torsion, grain growth behavior, mechanical alloying, and spark plasma sintering.

Hyoung Seop Kim received his BSc, MSc, and PhD degrees in 1986, 1988, and 1992, respectively, in Department of Metallurgical Engineering, Seoul National University. Prof. Kim is a Professor at Pohang University of Science and Technology (POSTECH) working in a broad area of physical metallurgy, specifically in unified constitutive modeling, porous materials, nanomechanics, high entropy alloys, severe plastic deformation, and architectured material designs. He has published more than 400 SCI-indexed papers scoring an h-index of 42.

individual elements.[33] Due to the ambiguity over the role of entropy in solid solution formation, a few research groups have suggested referring the HEAs as multi-principal element alloys (MPEAs), baseless alloys, concentrated solid solution alloys (CSAs), and compositionally complex alloys (CCAs).[6,30,34–40] Regardless of multiple phases or compound formation, it is worth mentioning that the significant concentration of various elements is present in the secondary phases/compounds. Besides, HEAs are established to have four inherent characteristics. (i) entropy effect – stabilizes the solid solution formation; (ii) lattice distortion effect – significantly influences the properties; (iii) sluggish diffusion effect – slows down the diffusion kinetics; (iv) cocktail effect – composite effect on final properties.[2,5,41,42]

Though HEAs are established to have sluggish diffusion effect, the experimental studies to elucidate the diffusion kinetics are rather limited.[43–46] Tsai et al.[43] investigated the interdiffusion coefficients in Cr–Fe–Co–Mn–Ni HEA system using quasi-binary approach. They concluded that diffusion coefficients were not sensitive to the composition and the normalized activation energies in HEAs are higher than those of reference metals. They ascribed the sluggish diffusion effect in HEAs to the large lattice potential energy fluctuation between the lattice sites which leads to the high normalized activation energy. Kulkarni et al.[44] investigated the interdiffusion in Cr–Fe–Co–Ni HEA system at 1000 °C and concluded that diffusional interactions should not be ignored while describing

the diffusion in HEAs. This finding is contrary to Tsai et al.[43] investigations where they concluded the single diffusion parameters are sufficient to explain the diffusion kinetics. Beke et al.[45] reanalyzed the diffusion coefficients of elements in CrMnFeCoNi HEA from the experimental data of Tsai et al.[43] and concluded that sluggish diffusion could be explained based on the correlation effects rather than high activation energies. They used the law of corresponding states to reanalyze the diffusion coefficients and confirmed the sluggish diffusion effect in HEAs as compared to the reference metals. Dabrowa et al.[46] used a combinatorial approach to simultaneously determine the tracer diffusion coefficients in Al–Cr–Fe–Co–Ni system in the temperature range of 1000–1100 °C. They validated the usage of combinatorial approach using the experimental data of Tsai et al. and concluded that diffusion coefficients of HEAs are significantly lower than conventional alloys. Vaidya et al. first measured the tracer diffusion of Ni in CrFeCoNi and CrMnFeCoNi HEAs using radiotracer technique in the temperature range of 800–1100 °C.[47] They reported that diffusion of Ni in both HEAs follow Arrhenius behavior and the tracer diffusion in HEAs becomes sluggish only if it is considered at homologous temperature but not at absolute temperature. They concluded that the diffusion in HEAs is not predictably sluggish, and factors such as energy barriers and frequency factors also contribute to slow diffusion rate in HEAs, but not solely from the configurational entropy. Zhang et al.[40] used a combined approach of experimental and computational methods to understand the diffusion kinetics in Al–Cr–Fe–Co–Ni and Cr–Mn-Fe–Co–Ni systems. They developed the mobility database of the Cr–Mn–Fe–Co–Ni system and further validated it by experimental data from their work and literature. They concluded that diffusion of Ni is not sluggish with increasing the number of components even with homologous temperature, which conflicts Mayur et al. observation.[47] The available literature on the diffusion studies of HEAs are not conclusive and requires a lot of investigations to elucidate the diffusion kinetics of HEAs.

Despite the formation of multiple phases and ambiguous over the role of entropy in the formation of solid solution, the literature has been flooded with investigations on HEAs (**Figure 1**) due to its unique alloy design and enhanced properties as compared to conventional alloys.

The need for the development of new materials with an outstanding microstructural stability and resistance to softening at high temperature for high-temperature applications has been one of the prime interests of materials scientists. In this regard, HEAs show a greater potential for many structural applications especially at extreme temperatures due to their distinctive properties such as strength retention at elevated temperatures, excellent thermal stability, age hardening behavior, remarkable fracture toughness at cryogenic temperature, and better wear and oxidation resistance.[6,10,37,41,42,48–73] For instance, the fatigue behavior of $Al_{0.5}CrFeCoNiCu$ HEA shows comparable fatigue endurance limit to ultimate tensile strength ratio with conventional alloys.[70] The AlCrMnFeNi HEA demonstrates excellent workability with the rolling extension of ≈4260% without any cracking.[41] The refractory HEAs possess remarkably very high yield strength at higher temperatures than those of conventional superalloys.[74] The $CrFeCo_{1.5}Ni_{1.5}Ti$ and
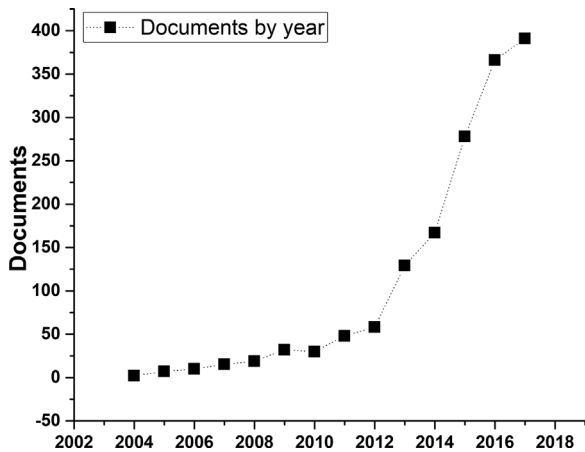
Figure 1. Year wise publications in the research area of HEAs (Based on the Scopus analyze search results for "High Entropy Alloys" as on Sep 12, 2017).

$Al_{0.2}CrFeCo_{1.5}Ni_{1.5}Ti$ HEAs exhibit better wear resistance than that of conventional wear-resistant steels.[69] The exceptional wear resistance in these two HEAs is attributed to the outstanding anti-oxidation property and resistance to thermal softening. The VCrMnFeCoNi HEA exhibits excellent cryogenic mechanical properties with a yield strength of ≈1 GPa and elongation up to 46%.[59] The HE nitride film of SiTiVAlCrNb shows remarkable thermal stability by retaining its nanostructure even after annealing at 1000 °C for 5 h.[75] The $Re_{0.21}Ru_{0.19}Rh_{0.20}Re_{0.21}Os_{0.22}Ir_{0.19}$ HEA shows remarkable phase stability under heat treatment up to 1227 °C and compression up to 45 GPa.[76] In addition, a wide range of multicomponent amorphous alloys based on equiatomic substitution has been investigated.[77–82] In one of the study, the addition of Nb is reported to increase the thermal stability of amorphous phase.[81] Zhang et al.[78] investigated the phase formation in (Ti, Zr, Nb)–(Cu, Ni)–Al equiatomic alloys and demonstrated a high thermal stability against crystallization with a large supercooled liquid region of over 125 K. Ma et al.[82] examined the glass forming ability in Ti–Zr–Hf–Cu–M (M = Fe, Co, Ni) alloys and reported that multicomponent amorphous alloys have better glass-forming ability than simpler alloy system.

The vast majority of literature indicates that HEAs have greater potential for high-temperature applications. In most of the studies, HEAs are developed with the aim of achieving a single phase with superior properties and compared with the conventional alloys based on the individual constituent elements. However, the studies on exploiting the advantage of the second phase in enhancing the properties are rather limited. By proper alloy design strategy, the second phase may provide the properties required for the high-temperature applications such as additional strengthening, resistance to grain growth, and softening at high temperatures, and excellent oxidation resistance.[83] For instance, Li et al.[84–86] developed a new class of transformation induced plasticity assisted dual phase $Fe_{50}Mn_{30}Co_{10}Cr_{10}$ HEA. The alloy consists of FCC matrix and laminate HCP phase in the as-homogenized state with the superior strength-ductility combination. They demonstrated that compositional homogeneity is an important factor to be considered in developing dual phase HEA with the excellent strength-ductility combination. He et al.[87,88] attempted to improve the tensile properties of HEAs by precipitation hardening through careful thermomechanical processing and microstructure control. They demonstrated the formation of coherent L12 precipitates in CrFeCoNi HEA by the addition of a minor amount of Al and Ti. This composite microstructure resulted in very high yield strength of over 1 GPa with ductility of 17%. Lu et al.[55] demonstrated a novel combination of high tensile ductility and fracture strength up to 700 °C by an innovative approach toward the alloy design using eutectic alloy concept, named as eutectic HEAs. They developed a eutectic-like microstructure which consists of an alternate layer of soft FCC and brittle BCC phases in $AlCrFeCoNi_2$ HEA. The alloy exhibited unusual work hardening behavior ($\sigma_{UTS}/\sigma_{0.2, YS} \approx 16$) as compared to the conventional alloys (≈3). The very high work hardening is attributed to the fine lamellar structure with an alternate layer of soft FCC and hard BCC phase. In a similar line, Wani et al.[89,90] attempted to enhance the mechanical properties of $AlCoCrFeNi_{2.1}$ alloy with duplex structure through thermo-mechanical processing and demonstrated a very high ultimate tensile strength of 1.2 GPa with a total elongation of ≈23%. He et al.[91] attempted to design eutectic HEAs based on $CoCrFeNiNb_x$ and suggested that $CrFeCoNiNb_{0.5}$ exhibits a remarkable combination of fracture strength and ductility, with compressive fracture strength and ductility of above ≈2.3 GPa and ≈40%, respectively. Shaysultanov et al.[92] fabricated a novel non-equiatomic $Fe_{36}Mn_{21}Cr_{18}Ni_{15}Al_{10}$ HEA with BCC/B2 dual-phase structure and demonstrated a high compression yield strength of ≈990 MPa up to 400 °C. Gwalini et al.[93] showed an excellent combination of mechanical properties (yield strength: ≈490 MPa, tensile strength: 850 MPa, and ductility: ≈45%) by optimizing and coupling the grain boundary strengthening and precipitation strengthening mechanisms. Zhang et al.[94] developed a new $AlTi_{0.5}Cr_{1.5}Fe_{1.5}CoNi$ HEA with dual-phase BCC structure and demonstrated an excellent combination of high yield strength and large plasticity under quasi-static compression. The alloy exhibited high yield strength of ≈2 GPa with a plastic strain greater than ≈30%.

Nanocrystalline (NC) metals are considered to have greater potential as structural materials at room temperature due to its unique and superior mechanical properties.[95–98] Despite its unique properties at room temperature, NC metals lose their potential at higher temperature due to grain boundary diffusion and sliding. Moreover, it has been reported that grain growth occurs at room temperature for few NC metals.[99,100] Due to their high vulnerability to grain growth at high temperatures and in some case at room temperature, their applications are rather limited. However, it is possible to retain the potential properties of NC materials at higher temperatures by utilizing the HEA design concept. Zou et al.[101] produced a stable NC NbMoTaW HEA with columnar grains of ≈70–100 nm grain size and demonstrated the retention of high yield strength of ≈5 GPa up to 600 °C. The NC NbMoTaW HEA exhibited consistent strain rate sensitivity of ≈0.005 from room temperature to 600 °C. The alloy has very high strength to density ratios and strength normalized by shear modulus than any other reported studies on NC metals at the same homologous temperature. Zhou et al.[53] utilized the concept of reducing the

grain boundary energy by grain boundary high entropy effects and developed a thermally stable NC HEA. They demonstrated remarkable thermal stability in Ni-containing NC HEAs, which outperformed Ni-based binary NC alloys. The NC $Cr_{23}Fe_{23}Co_{23}Ni_{25}Zr_2Nb_2Mo_2$ HEA, synthesized by mechanical alloying (MA), exhibited stable grain sizes of ≈ 13, 36, and ≈ 56 nm after annealing at 600, 900, and 1000 °C, respectively (**Figure 2**). However, significant grain growth was observed in NC CrFeCoNi HEA without any high-entropy grain boundary complexions. This observation imparts the significance of grain boundary high entropy effect on thermal stability of NC HEAs. They concluded that both thermodynamics and kinetics effects contribute to the stabilization of NC HEAs. Praveen et al.[102] demonstrated an exceptional resistance to grain growth in NC CrFeCoNi HEA at a high homologous temperature of $\approx 0.68\, T_m$ for a prolonged duration of 600 h. They observed that the average grain size of CrFeCoNi HEA increased from ≈ 120 to 260 nm after heat treatment at 900 °C for 600 h They attributed the enhanced grain growth resistance to the formation of composite microstructure, due to the unsolicited contamination during processing. The recent overview article by Chokshi[103] on high-temperature deformation in fine-grained HEAs discusses the possible high-temperature deformation mechanisms and also highlights the deformation mechanism maps in fine-grained HEAs.

Even though HEAs have the potential to be a high-temperature material, a detailed literature survey on HEAs indicates that vast majority of the studies are focused on room temperature properties. Although the high-temperature studies on HEAs are limited, the available literature on HEAs suggests that with proper alloy design it is possible to produce thermally stable HEAs with a potential to replace superalloys shortly. Suitable HEA design strategies regarding choosing the elements are vital for different industrial applications. Currently, several review articles on HEAs[6,37,41,42,62–66,104–107] and two books[5,108] have been published with the focus on HEAs progress, solid solution formation rules, and a critical assessment of the fundamental principles of HEAs. In contrast, the current review article imparts the outstanding properties of HEAs as a potential candidat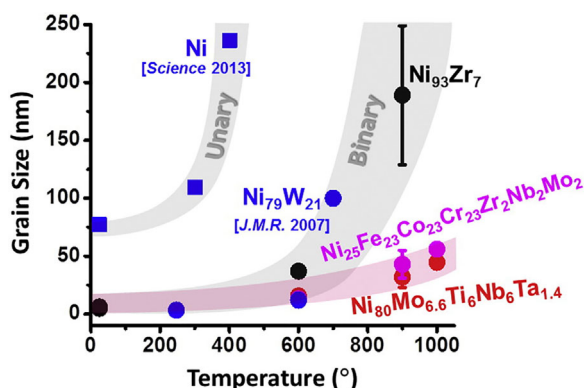e for high-temperature applications and also highlights the need for a profound research work on the high-temperature behavior of HEAs. The current article will provide a systematic knowledge and insight into the available literature on phase stability, microstructural stability, and high-temperature mechanical properties of HEAs. This article will be highly beneficial for the materials science community with the focus on the development and understanding of HEAs for high-temperature applications.

In the literature, the elements representing the alloys are arranged based on the atomic number, alphabetic order, and sometimes in a random order. In the present article, the elements are written in the order of increasing atomic number to represent the alloys for better understanding and consistency.

2. Commonly Studied Alloys

In the very initial stage of HEA research field, $Al_xCrFeCoNiCu$ HEAs have received wide attention due to its unique properties in comparison to conventional alloys, especially the strength retention of $Al_{0.5}CrFeCoNiCu$ HEA till 800 °C.[4,27,109–115] The variation of the compressive yield strength at different temperatures is shown in **Figure 3**. However, the segregation of Cu was observed in Cu containing HEAs due to its high enthalpy of mixing with other elements.[21,27,111,116] Besides, the modification of Al content has led to the significant changes in microstructure and mechanical properties of AlCrFeCoNi HEA.[109,117,118] For example, the alloy forms a single FCC phase when the Al content is less than a 0.45-mole fraction and single BCC phase when the Al content is more than a 0.9-mole fraction. Due to Cu segregation and the influence of Al on microstructure and mechanical properties, researchers shifted their focus to $Al_xCrFeCoNi$ HEA system, alloys without Cu.[119–123]

CrMnFeCoNi HEA, also known as Cantor alloy, has been the alloy of interest of late due to the formation of a single phase with enhanced mechanical properties, particularly at the cryogenic temperature.[57,124–131] It is worth mentioning that the recent studies on CrMnFeCoNi HEA have revealed the formation of
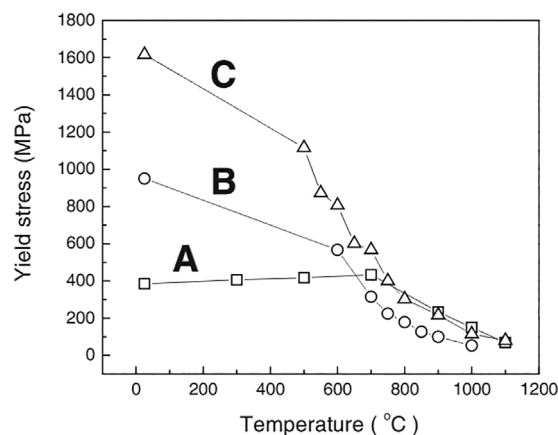

Figure 2. Exceptional resistance to grain growth in $Cr_{23}Fe_{23}Co_{23}Ni_{25}Zr_2Nb_2Mo_2$ HEA by utilizing the concept of grain boundary energy reduction. Reprinted from ref.[53] with permission from Elsevier, 2017.

Figure 3. Compressive yield stress as a function of temperature illustrating the strength retention of $Al_{0.5}CoCrFeNiCu$ HEA up to 800 °C [A: $Al_{0.5}$, B: $Al_{1.0}$, C: $Al_{2.0}$]. Reprinted from ref.[4] with permission from Wiley.

secondary phase during annealing in the intermediate temperature range.[30,31,132] On the other hand, HEAs made up of refractory elements have been the topic of interest for high-temperature applications. Refractory HEAs possess very high strength with strength retention at elevated temperatures.[74,133–138] Consequently, in the present article, the microstructural evolutions after heat treatment and mechanical behaviors at high temperatures of $Al_x CrFeCoNi$ HEAs, CrMnFeCoNi HEA, and refractory HEAs are summarized. Concurrently, the high-temperature properties of other HEAs and other high-temperature properties such as high-temperature oxidation and hot corrosion resistance cannot be overlooked, and are eventually included at the end of this review article.

3. AlxCrFeCoNi

$Al_x CrFeCoNi$ HEAs' variant shows structural changes from FCC to BCC with increasing Al content.[27,117,118,139–143] The structure varies from single FCC phase ($Al_{0–0.3}$) to mixed FCC and BCC phase ($Al_{0.5–0.9}$), and then finally to single BCC phase ($Al_{0.9–3}$). The BCC phase in these alloys is composed of disordered BCC (A2) and ordered BCC (B2) due to the spinodal decomposition.[27,117,118] Ogura et al.[139] elucidated the effect of Al content on phase transition using first principles electronic structure calculations. They observed the total energy difference between FCC and BCC decreases with increasing Al content. They concluded that the transition from FCC to BCC with increasing Al content is mainly due to the large energy gain by the DO_3 structure with the addition of Al. Also, the calculations indicate that Cr and Fe tend to stabilize the BCC structure, while Ni and Co favor the FCC structure.

Like variation in the crystal structure, the microstructure of the as-cast alloys also varies with Al content.[118,142] The as-cast microstructure changes from the columnar cellular structure ($Al_{0–0.3}$) to columnar dendritic structure ($Al_{0.4–0.6}$), then to equiaxed nondendritic grain ($Al_{0.7–0.8}$), then to equiaxed dendritic grain ($Al_{0.9–1.5}$), and finally to non-equiaxed dendritic grain structure ($Al_{1.8–2.0}$).[118] The spinodal decomposition with different spinodal structure is observed for alloys with Al content above 0.5-mole fraction. The spinodal structure changes from interconnected and modulated phase structure ($Al_{0.5–1.0}$) to the uniform dispersion of spherical particles ($Al_{1.2–2.0}$). Sistla et al.[144] varied the Al/Ni ratio and fabricated a thin-walled HEA components using laser-aided direct metal deposition. They reported that the Al/Ni ratio has a significant effect on phase transformation, microstructure, and hardness of $Al_x CrFeCoNi_{2–x}$ HEAs. They observed that the addition of Al causes the simultaneous occurrence of spinodal decomposition and ordering in this alloy. The alloy with Al: Ni ratio of 0.7: 1.3 exhibited a good combination of hardness and strength due to the precipitation of B2 phase. The $Al_{0.1} CrFeCoNi$ HEA, produced by vacuum levitation melting, exhibited a very high impact toughness of ≈371 J at cryogenic temperature.[145] The impact toughness of this alloy is observed to increase with decreasing temperature from 294 J at 25 °C to 371 J at cryogenic temperature. The increased activity of nano-twinning during plastic deformation and the formation of the high density of smaller dimple at fracture surfaces are attributed for the high impact toughness.

Li et al.[146] fabricated $Al_{0.3} CrFeCoNi$ HEA fibers with diameters ranging from 1–3.15 mm by the hot-drawing process and demonstrated enhanced mechanical properties at cryogenic temperature as compared to room temperature. The $Al_{0.3} CrFeCoNi$ HEA fiber with 1 mm diameter exhibited a remarkable combination of strength and ductility at both room temperature and cryogenic temperature due to the presence of B2 precipitates and fine grain size (1207 MPa and 7.8% at room temperature, 1600 MPa and 17.5% at cryogenic temperature). They concluded that the enhanced properties at cryogenic temperature are mainly due to the change in deformation mechanism from a planar slip at room temperature to the deformation induced nanoscale twinning at cryogenic temperature. The melting point of $Al_x CrFeCoNi$ HEAs shows complex behavior with the variation of Al. The melting point decreases from ≈1400 °C at x = 0 to ≈1350 °C at x = 0.7, and then increases to ≈1400 °C at x = 1.8.[142]

3.1. Microstructural Evolution After Heat Treatment

The high-temperature XRD experiments demonstrate that the crystal structure of $Al_x CrFeCoNi$ HEA system, except for $Al_{0.9–1.2}$ alloys, remains stable in the temperature range of 200–1100 °C.[142] In $Al_{0.9}$–$Al_{1.2}$ HEAs, which has a BCC structure in the as-cast condition, the formation of FCC phase was observed above 600 °C. In addition to FCC phase, sigma phase (σ) was also observed in the temperature range of 600–900 °C. The microstructural features of $Al_x CrFeCoNi$ HEA remained unchanged after heat treatment, except for the coarsening of features size in all alloys and the appearance of acicular precipitates in $Al_{0.5}$ HEA. The microstructural evolution after heat treatment of as-cast alloy at 900 and 1100 °C are shown in **Figure 4**. Munitz et al.[147] investigated the effect of heat treatment impact on the microstructure and mechanical properties of AlCrFeCoNi HEA. The alloy consisted of BCC and B2 phase in the as-cast condition. They observed that the BCC phase transforms to σ phase after heat treatment at 850 °C and the σ phase changes back to BCC phase after heat treatment at 975 °C. The formation of FCC phase was also observed after heat treatment at 850 °C and disappeared after heat treatment at 1200 °C. The spinodal decomposition was found to occur in both dendritic and inter-dendritic regions after heat treatment at 1100 and 1200 °C. Liu et al.[148] investigated the effect of processing conditions on the phase stability of AlCrFeCoNi HEA. They observed that structure changes from BCC and B2 to BCC and FCC phases in AlCrFeCoNi HEA with and without cold rolling after heat treatment at 950 °C for 4 h.

Butler et al.[149] meticulously coupled the CALPHAD (Computer Coupling of Phase Diagrams and Thermochemistry) based predictions using ThermoCalc and experimental observations to investigate the phase stability of $Al_x CrFeCoNi$ HEAs (x = 0.5, 0.75, 1, and 1.5). The microstructural evolution in $Al_x CrFeCoNi$ (x = 0.5, 0.75, 1, and 1.5) after prolonged exposure at 700 °C for 1000 h and at 1050 °C for 520 h followed by water quenching are summarized in **Table 1**.[149] In all the cases, the sample annealed at higher temperature produced coarsened microstructure, and the B2 phase was enriched in Ni–Al, the BCC phase was rich in Cr, the FCC phase was Al-deficient, and
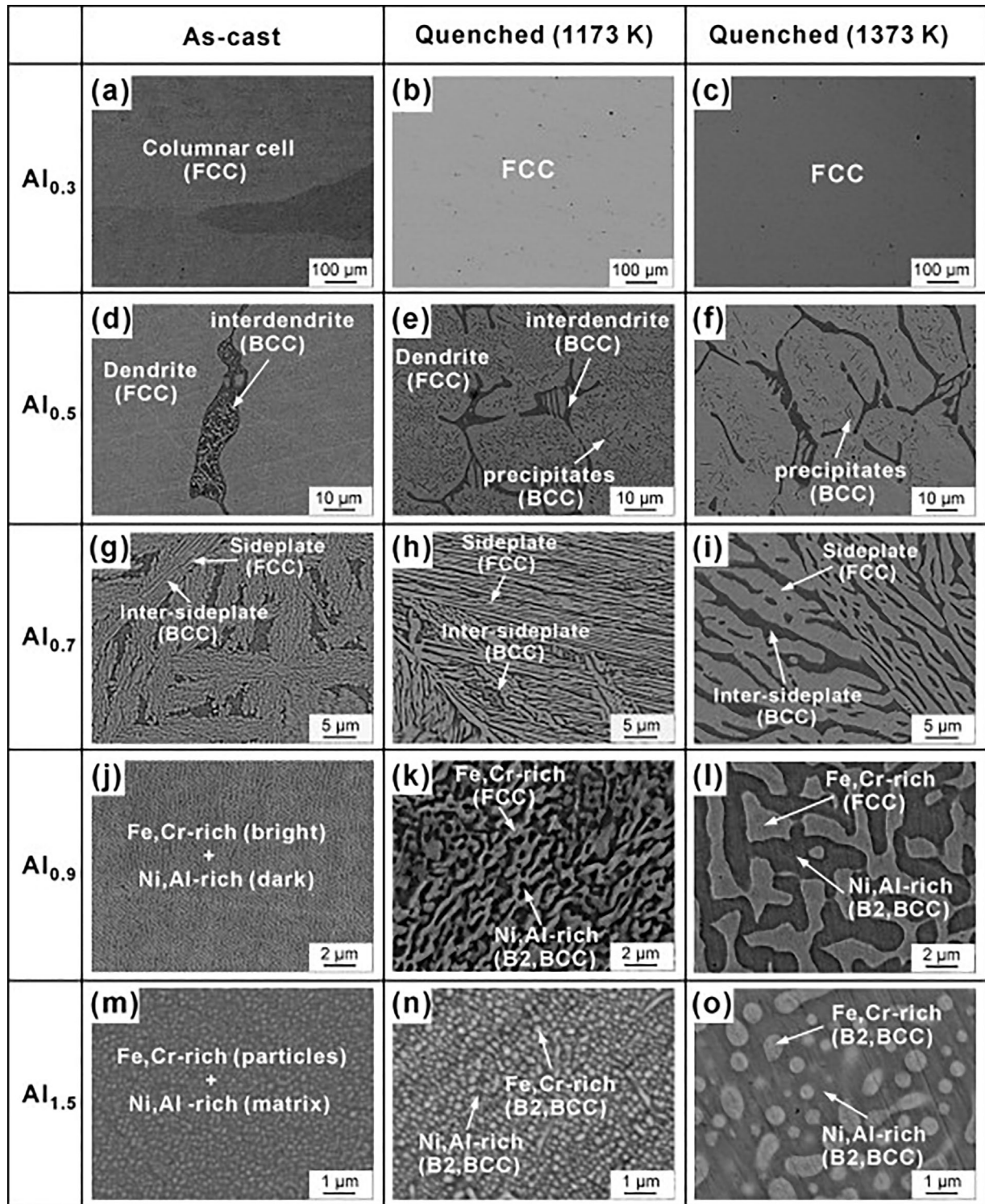
Figure 4. SEM BSE micrographs of as-cast and heat-treated microstructures for AlxCrFeCoNi HEAs with varying Al content. Reprinted from ref.[142] with permission from Elsevier.

the σ phase was rich in Fe and Cr. The phase predicted by the model was in good agreement with the experimental observations in $Al_{0.5}CrFeCoNi$ and $Al_{30}CrFeCoNi$ HEAs. However, the model failed to predict the phases in other alloys accurately. For instance, the model did not predict the formation of FCC phase at 700 °C in $Al_{0.75}CrFeCoNi$ HEA. In AlCrFeCoNi HEA, the model predicted the formation of B2 and sigma phase at 700 °C which is significantly different from the experimental

Table 1. The phase formation in AlxCoCrFeNi at different conditions.[149]

HEA	As-cast	700 °C–1000 h	1050 °C–520 h
Al$_{0.5}$CoCrFeNi	B2/BCC + FCC	B2/BCC + FCC + σ	FCC + B2/BCC
Al$_{0.75}$CoCrFeNi	B2/BCC + FCC	B2/BCC + FCC + σ	FCC + B2/BCC
AlCoCrFeNi	B2/BCC	B2/BCC + FCC + σ	B2/BCC + FCC
Al$_{1.5}$CoCrFeNi	B2/BCC	B2/BCC	B2/BCC

observation, and it failed to predict the formation of FCC phase at 1050 °C. The predicted phase formation using CALPHAD based thermodynamic modeling was only semi-consistent with the experimental observations. This indicates an inaccuracy of the current thermodynamic database and the necessity for the improvement of the current thermodynamic database.[140]

Zhang et al.[150] studied the phase stability of different variant of AlCrFeCoNi HEAs by integrating the phase diagram calculation with the experimental investigations. The discrepancies observed between the predictions and experimental results are mainly due to the short periods of heat treatments in the experimental studies. They concluded that the short duration of annealing/heat treatment is not sufficient for the alloy to form an equilibrium phase, especially at lower temperatures. For example, a single FCC phase was observed when the hot isostatically pressed Al$_{0.3}$CrFeCoNi HEA were heat treated at 700 °C for 100 h; however, nano-sized B2 precipitates were seen in addition to FCC phase when the duration of heat treatment was increased over 200 h. In another study, the composition-decomposition in CoCrFeNi alloy occurred when annealed at 750 °C for 800 h. However, the composition-decomposition was observed in shorter duration when the minor content of Al was added to CrFeCoNi HEA.[151]

The as-cast Al$_{0.3}$CrFeCoNi HEA consists of spherical nano-precipitates with L1$_2$ ordered structure in the FCC matrix.[152] The morphology of these spherical precipitates changes to platelets when annealed at 700 °C for 72 h, while the both morphology and structure change to rod-shaped precipitates and B2 structure, respectively, when annealed at 900 °C for 72 h. The Al$_{0.3}$CrFeCoNi HEA forms a single FCC phase after solutionizing at 1200 °C for 30 min followed by water quenching.[153] Subjecting the solutionized sample to heat treatment at 500 °C for 150 h and 700 °C for 50 h resulted in the formation of fine ordered L1$_2$ and coarse B2 precipitates, respectively. The B2 precipitates have a lath-like morphology and exhibit orientation relationship with the FCC matrix. Remarkably, the addition of Cu and removal of Co from the alloy have increased the stability of L1$_2$ precipitates in Al$_{0.3}$CrFeNi$_2$Cu HEA.[153,154] The precipitates were observed to be stable at both 550 and 700 °C, with an increase in precipitate size from 5 nm at 550 °C to 50 nm at 700 °C. The B2 precipitates were observed to form primarily along the grain boundaries during annealing of cold rolled Al$_{0.3}$CrFeCoNi at 800–1000 °C for 1 h.[155] The presence of B2 precipitates effectively prevents the grain coarsening during recrystallization by pinning the grain boundary, resulting in an ultrafine-grained microstructure. The average grain size of the sample recrystallized at 1000 and 1050 °C were 0.7 and 52.8 μm, respectively. The rapid grain growth during annealing at 1050 °C

is attributed to the dissolution of B2 precipitates above 1000 °C. A similar observation was reported for Al$_{0.5}$CrMnFeCoNi HEA.[156] In thermomechanical processed Al$_{0.5}$CrMnFeCoNi HEA, the morphology of BCC was primarily globular and occasionally appeared in the form of large blocks or bands along the grain boundaries of equiaxed FCC grains.[156] The presence of BCC phase along the grain boundaries provides a pinning effect and prevents grain coarsening during heat treatment. However, the volume fraction of BCC phase decreases with increasing annealing temperature above 1000 °C, resulting in a significant grain growth.

The grain size greatly influences the annealing-induced phase transformation of L12 to the B2 structure in Al0.3CrFeCoNi HEA.[157] In coarse grain (CG) HEA, the formation of B2 phase was preceded by the formation of L1$_2$ phase, while the B2 phase forms directly without L1$_2$ formation in NC HEA.[157] Also, the formation of B2 phase occurs relatively at a lower temperature in NC HEA than CG HEA. The difference in phase transformation and kinetics is attributed to the difference in elemental diffusivity in CG and NC materials. The formation of L1$_2$ phase requires a short-range elemental diffusion, while the long-range elemental diffusion is needed for the formation of B2 phase. Thus, the formation of L1$_2$ is kinetically more favorable than the formation of B2 phase at a lower temperature. In contrast, the presence of high volume fraction of grain boundary in NC HEA provides the diffusion pathway even at low temperature and thereby favor the formation of B2 phase directly without the formation of any transition phase.

The in-situ TEM study reveals the formation of two different types of precipitates: Cr-rich σ phase (CrFe type) and Al-rich θ phase (Al$_{45}$Cr$_7$ type) in Al$_{0.7}$CrFeCoNi HEA after annealing at 900 °C for 10 min.[140] The formation of σ phase is proposed to occur either by three-step formation or directly from the FCC matrix. In the three-step formations, the Cr-rich BCC phase nucleates first in the B2 region and the σ phase forms at the B2/BCC interface followed by the decomposition of BCC phase. The formation of secondary phase is reported to occur at 500 °C, and it is reversible to a certain extent. The volume fraction of the secondary phase increases with increasing temperature and decreases with decreasing temperature in Al$_{0.3}$CrFeCoNi HEA.[140] Wani et al.[90] attempted to refine the microstructure of AlCoCrFeNi$_{2.1}$ eutectic HEA by severe cold-rolling followed by annealing. They observed that the severe cold rolling of as-cast AlCoCrFeNi$_{2.1}$ eutectic HEA, with a fine eutectic mixture of L1$_2$ and B2 phases, resulted in disordering of L1$_2$ phase. The annealing of severely deformed alloy has led to the formation of duplex microstructures with equiaxed morphologies. This duplex microstructure exhibited significant resistance to grain growth with the average grain size of 0.5, 0.7, and 2.0 μm after annealing at 800, 1000, and 1200 °C for 1 h, respectively.

3.2. Age Hardening Behavior

The addition of minor alloying elements such as C, Mo, and Ti have shown a significant effect on the aging behavior of Al$_{0.3}$CrFeCoNi HEA (**Figure 5**).[158,159] The hardness of Al$_{0.3}$CrFeCoNi HEA increases by ≈65% after aging at 700 °C for 144 h, and the addition of Mo and Ti in minor amount has
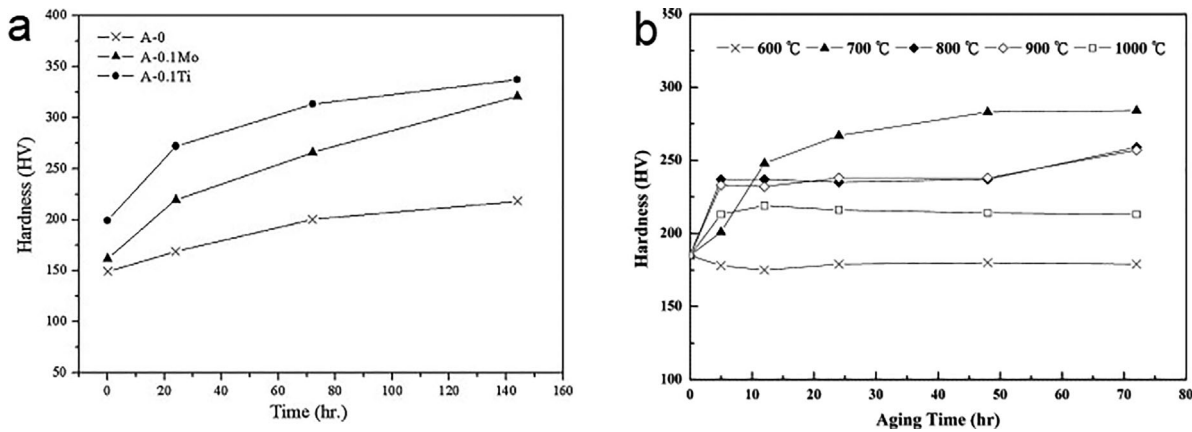
**ADVANCED
SCIENCE NEWS**

www.advancedsciencenews.com

**ADVANCED
ENGINEERING
MATERIALS**

www.aem-journal.com

Figure 5. Hardness variation with time illustrating the age hardening behavior of a) $Al_{0.3}CoCrFeNi$ (A–0), $Al_{0.3}CoCrFeNiMo_{0.1}$ (A–0.1 Mo), and $Al_{0.3}CoFeNiTi_{0.1}$ (A–0.1Ti) at 700 °C, and b) $Al_{0.3}CrFeCoNiC_{0.1}$ at different temperatures. Reprinted from refs.[158; 159] with permission from Elsevier.

increased the hardness by ≈83% and 89% in $Al_{0.3}CrFeCo$-$NiMo_{0.1}$ and $Al_{0.3}Ti_{0.1}CrFeCoNi$, respectively. The formation of (Ni, Al) rich B2, (Ni, Co, Ti) rich B2 are attributed to the hardness increase after aging in $Al_{0.3}CrFeCoNi$ and $Al_{0.3}CrFeCoNiTi_{0.1}$ HEAs, respectively. The addition of Mo has resulted in the formation of σ sigma phase in addition to B2 precipitates and resulted in the hardness increase by ≈89%. The addition of carbon has led to the formation of Cr_7C_3 carbide in as-cast $Al_{0.3}CoCrFeNiC_{0.1}$ HEA. The Cr_7C_3 carbide transforms to $Cr_{23}C_6$ carbide after aging treatment in the temperature range of 700–800 °C. The change in carbide structure has resulted in the hardness increase (Figure 5), and the optimal age hardening is achieved at 700 °C for 70 h. The B2 precipitates are observed in the temperature range of 800–1000 °C and contribute to an additional hardening effect.

The high-pressure torsion (HPT) of as-cast $Al_{0.3}CrFeCoNi$ HEA has a significant influence on the age hardening behavior.[160] The HPT process refines the grain size from ≈350 μm to ≈30 nm. As stated in the preceding section, the B2 precipitation occurs at a lower temperature in the sample with fine grains (HPT-processed) than the sample with coarse grains (as-cast). As a consequence, the age hardening behavior is observed at a lower temperature (≈400 °C) than that of the as-cast sample (≈500 °C) (**Figure 6**). Also, the peak hardness of HPT-processed sample is approximately four times higher than that of the as-cast sample. The very high hardness of the HPT-processed sample is attributed to the presence of fine B2 phase as compared to the coarse B2 phase in the cast sample.

Similar to the effect of HPT processing, a minor modification of the alloy composition also significantly influences the age hardening behavior. For instance, replacing the Co with Cu and increasing the Ni content resulted in 72% increase in hardness of $Al_{0.3}CrFeCuNi_2$ after annealing at 550 °C for 150 h.[153] It is worth mentioning that the hardness increase in $Al_{0.3}CrFeCoNi$ HEA are only ≈42% after annealing at 550 °C for 150 h. Also, high hardness is achieved for $Al_{0.3}CrFeCuNi_2$ HEA at all aging conditions than that of $Al_{0.3}CrFeCoNi$ HEA.

In another example, $Al_xCrFe_{1.5}MnNi_{0.5}$ [x = 0.3 and 0.5] HEAs are designed with an objective of producing a cheaper alloy with enhanced properties.[161] The alloys exhibit significant

age-hardening phenomenon at higher temperatures, and the peak hardness of ≈HV 850–890 is achieved at 600 °C for 100 h. The age-hardening phenomenon in these alloys is attributed to the precipitation of B2 and σ phase ($Cr_5Fe_6Mn_8$ with tetragonal structure).[161,162] Also, the $Al_xCrFe_{1.5}MnNi_{0.5}$ alloy exhibits better oxidation resistance up to 800 °C. A detailed TEM investigation on $Al_{0.3}CrFe_{1.5}MnNi_{0.5}$ HEA reveals that BCC phase transforms to σ phase through the diffusionless transformation without altering its composition, rather than forming by precipitation.[163] Thus, the significant age hardening behavior in $Al_{0.5}CrFe_{1.5}MnNi_{0.5}$ HEA is attributed to the phase transformation from BCC to σ phase, and not because of precipitation hardening. The similar behavior of BCC to σ phase transformation has also been observed in $Al_{0.5}CrNiCoTi_{0.5}$ HEA during aging treatment.[164]

The $Al_{0.5}CrFeCoNi$ HEA demonstrated an increase in yield strength and ultimate strength with the aging treatment at 650 °C for 30 min to 8 h, but with the reduction in ductility.[165] The yield strength of ≈714 MPa and ultimate strength of ≈355 MPa in as-cast condition increased to 1220 and 834 MPa, respectively, after aging treatment for 8 h. The formation of
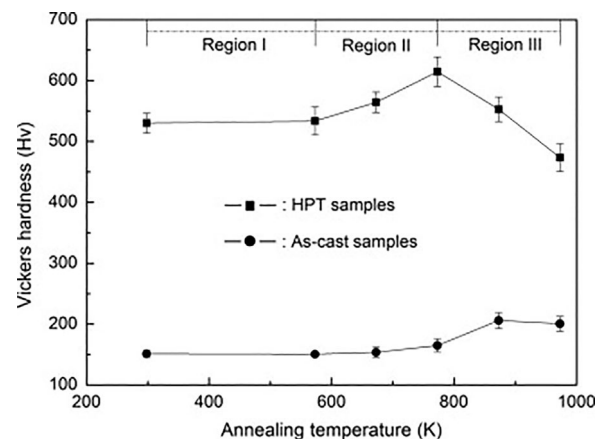

Figure 6. Age hardening behavior of the as-cast and HPT-processed $Al_{0.3}CrFeCoNi$ HEAs. Reprinted from ref.[160] with permission from Elsevier.

ADVANCED
SCIENCE NEWS

www.advancedsciencenews.com

ADVANCED
ENGINEERING
MATERIALS

www.aem-journal.com

nano-sized precipitates (≈18 nm) in FCC phase and B2 precipitates (≈70 nm) in BCC phase is attributed to the increase in strength and the reduction in ductility. The annealing of as-cast $Al_{0.3}$CrFeCoNi HEA has a significant effect on the mechanical properties due to the formation of $L1_2$ fine precipitates at 700 °C and B2 coarse precipitates at 900 °C.[152] The yield strength increases from ≈175 MPa in the as-cast condition to ≈300 and ≈250 MPa after annealing at 700 and 900 °C, respectively, and significant work hardening is observed for the alloy annealed at 900 °C. The presence of fine nano $L1_2$ precipitates and coarse B2 precipitates are attributed to the high yield stress at 700 °C and large work hardening at 900 °C, respectively. The alloy with ultrafine-grain size, achieved by thermomechanical treatment, exhibit an excellent combination of ultimate tensile strength (>1000 MPa) and ductility (>40%).[155] It is reported that the effect of B2 precipitates on yield strength is not significant and the major strengthening contribution comes from the grain boundary strengthening. Wang et al.[166] investigated the effect of $L1_2$ precipitates on tensile behavior of $Al_{0.2}$CrFeCoNi$_2$Cu$_{0.2}$ HEA. They fabricated the alloy with two different microstructures ($L1_2$ precipitates + FCC matrix, single FCC phase) and identical grain size by annealing the cold rolled alloy at various conditions. They observed that the presence of $L1_2$ nanoprecipitates increases the yield strength and ultimate tensile strength by 56 and 43%, respectively, without compromising on elongation to fracture. The dislocation shearing of $L1_2$ precipitates during tensile test resulted in the formation of crystallographically aligned slip bands. They concluded that the enhanced properties in the alloy with precipitates is mainly due to the formation of dynamic slip band refinement.

3.3. Mechanical Properties at Elevated Temperature

Yang et al.[167] investigated the deformation mechanisms of $Al_{0.1}$CrFeCoNi HEA at different temperatures in the range of 25–700 °C. The alloy, fabricated by vacuum induction melting followed by hot isostatic pressing, consists of single FCC phase with a coarse grain size of greater than 1 mm. The alloy exhibited a strong temperature dependence of yield strength and ultimate tensile strength (**Figure 7**). The yield strength and ultimate tensile strength decreases with increasing temperature. In contrast, the elongation to fracture increases up to 500 °C and then decreases with increasing temperature. The dislocation glide act as a primary deformation mechanism at room temperature and 500 °C. At 600 and 700 °C, the dissociation of dislocations and the motion of Shockley partials serve as an additional deformation mechanism and also lead to the formation of numerous stacking faults. Since the dissociation of partial dislocation decreases the dislocation density and reduces the barrier to dislocation movement, the work hardening phenomenon decreases at higher temperatures, and consequently, it promotes the early onset of necking instability. Zhang et al.[168] investigated the hot deformation behavior of $Al_{0.5}$CrFeCoNi HEA in as-cast and homogenized condition. In both the conditions, the flow stress increased with increasing strain rate and decreasing temperature. However, high flow stress was observed for the homogenized state than the as-cast
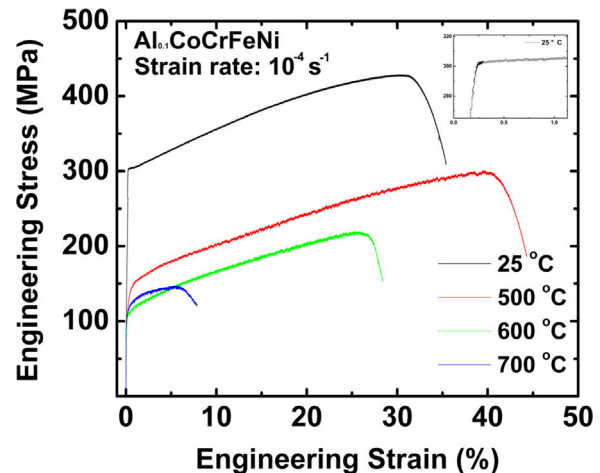

Figure 7. Engineering stress–strain curves of $Al_{0.1}$CoCrFeNi HEA at different temperatures and a strain rate of $10^{-4}\,s^{-1}$. The inset shows the magnified part of the curve after yielding at room temperature. Reprinted from ref.[167] with permission from Elsevier.

condition under the same deformation conditions. The average activation energy, which indicates the degree of obstruction to plastic deformation, was estimated to be ~300 kJ mol^{-1}. The optimum condition for thermomechanical processing of homogenized sample was identified as 945–965 °C and $10^{-1.7}$–$10^{-1.1}\,s^{-1}$. Chen et al.[169] observed a change in crystal structure in $Al_{0.5}$CrFeCoNiCu HEA after compression test in the temperature range of 400–600 °C at a strain rate of $5 \times 10^{-5}\,s^{-1}$. A single FCC phase and the mixture of FCC and BCC phases were observed for the samples tested at 400–500 °C and 600 °C, respectively. Consequently, the $Al_{0.5}$CrFeCoNiCu HEA showed higher yield strength at 600 °C than the samples tested at other temperatures.

Munitz et al.[147] investigated the impact of heat treatments on the mechanical properties of AlCoCrFeNi HEA. They reported that the alloy in as-cast condition consisted of FCC and B2 matrix with BCC precipitates in the dendritic region, while the interdendritic region consisted of BCC matrix with B2 precipitates. The hardness of the dendritic region remains the same after heat treatment at 850–1100 °C and increases after heat treatment at 1200 °C. In contrast, the hardness of ID region increased after heat treatment at 850 °C followed by a decrease in hardness till 1100 °C and then increase in hardness after heat treatment at 1200 °C. The increase in hardness of interdendritic region at 850 °C is attributed to the transformation of BCC to σ phase, and the decrease above 850 °C is attributed to the transformation of σ phase to BCC phase. The increase in hardness at 1200 °C in both the dendritic and interdendritic region is attributed to the formation of nano-precipitates because of spinodal decomposition. They observed a unique combination of compressive mechanical properties (yield strength ≈1450 MPa, UTS ≈2500 MPa, strain ≈20%) in AlCrFeCoNi HEA heat-treated at 1100 and 1200 °C due to spinodal decomposition and formation of nano-sized precipitates. **Figure 8** illustrates the compressive stress vs. strain curve for AlCrFeCoNi alloy in as-cast condition and after different heat treatments. They concluded that the homogenization temperature for this alloy
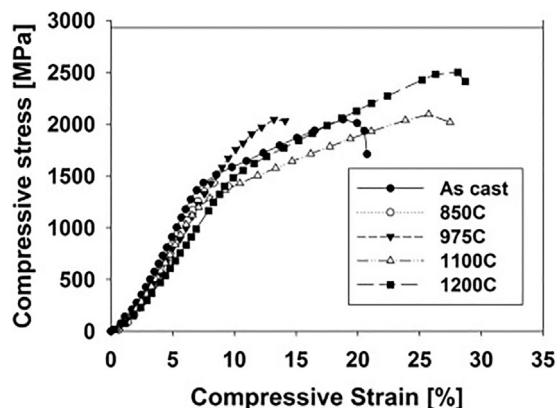
Figure 8. Compressive stress vs. strain curve for AlCrCoFeNi HEA after different annealing temperatures. Reprinted from ref.[147] with permission from Elsevier.

should be above 1200 °C as the majority of the phases are dissolved at this temperature, and the spinodal decomposition during cooling from 1200 °C bring out the better mechanical properties.

The hot hardness of Al_xCrFeCoNi HEAs decreases slowly with increasing temperature below ≈500 °C, and decreases rapidly above 500 °C, except for $Al_{0-0.3}$ alloys in which the hardness decreases slowly even above 500 °C (shown in **Figure 9**).[142] The $Al_{0-0.3}$ alloys exhibit higher resistance to softening than other alloys with different Al content. The age hardening behavior was observed for $Al_{0.9-1.0}$ alloys in the temperature range of 700–800 °C due to the formation of σ phase. The hot hardness transition temperature in this alloy system occurs at ≈0.5 T_m, which is comparable to In718, In718H, and T-800 commercial alloys. The indentation-creep performed in the temperature range of 500–900 °C indicates that slip and creep act as the main deformation mechanism below and above the transition temperature, respectively, for Al_x alloys with x > 0.5.[142] In
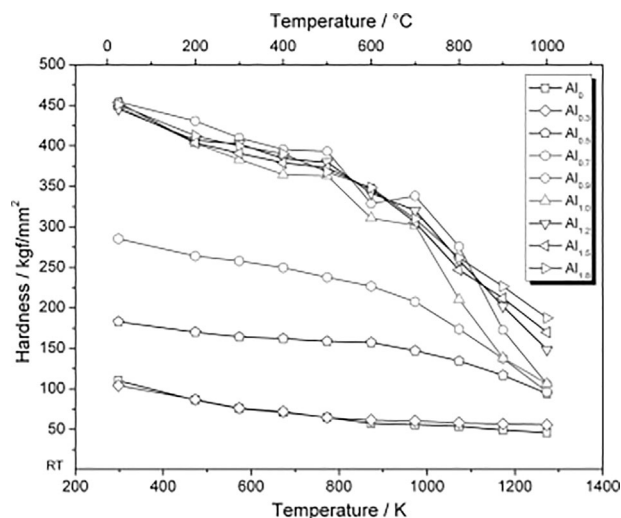
$Al_{0.3}$ alloy, no creep occurs and the slip act as the main deformation mechanism below and above the transition temperature. In $Al_{0.7-1.5}$ alloys, no creep deformation occurs below 600 °C, and the creep deformation occurs above 700 °C. In $Al_{0.5}$ alloy, no creep occurs at 800 °C due to the acicular precipitation in the dendritic phase. In another example, AlFeCoNiMo$_{0.5}$Cr$_x$ (x = 0–2) HEAs exhibit superior hot hardness and softening resistance than that of Inconel 718 (In718), precipitation hardened Inconel 718 (In718H), and Cobalt-based superalloys (T-800).[170]

The serrations in flow behavior have been reported for few HEAs.[169,171–174] Serrations, in general, can occur in flow curve during plastic deformation due to many factors, and one of them is the interaction between solute atoms and dislocations. The $Al_{0.5}$CrFeCoNiCu HEA shows the directional transformation of serrations from upward serrations at 400–500 °C to downward serrations at 600 °C (shown in **Figure 10**).[169] The critical strain for the onset of serrations in this alloy shows normal behavior, that is, the critical strain value decreases with increasing temperature. It is speculated that the dynamic strain aging (DSA) causes serration in this alloy. In another study, Al is reported to play a crucial role in DSA of $Al_{0.3}$CrFeCoNi HEA single crystals at 600 and 800 °C, as the serration was not observed in CoCrFeNi single crystals.[173]

The transformation of serration type from type A to type A + B and finally into type B + C with increasing temperature (200–500 °C) and decreasing strain rate (10^{-3}–10^{-4} s^{-1}) was observed in $Al_{0.5}$CrFeCoNi HEA with dual phase (FCC and BCC).[171] The elongation to fracture and tensile strength decreased with an increase in temperature. The reduction in elongation to fracture is attributed to the dynamic strain aging phenomenon because the solute atoms can hinder the movement of dislocations by interacting with them. Due to higher diffusivity at a higher temperature, the solute atoms can dynamically cluster around the dislocations and reduces the ductility at a higher temperature. However, the reason for embrittlement at high temperature is still an open question and needs elaborate study.

In summary, the formation of precipitates and phase transformation in Al_xCrFeCoNi HEA system play a significant role in mechanical properties at elevated temperatures and after

Figure 9. Hot hardness variation of Al_xCrFeCoNi [x = 0–1.8] HEAs. Reprinted from ref.[142] with permission from Elsevier.
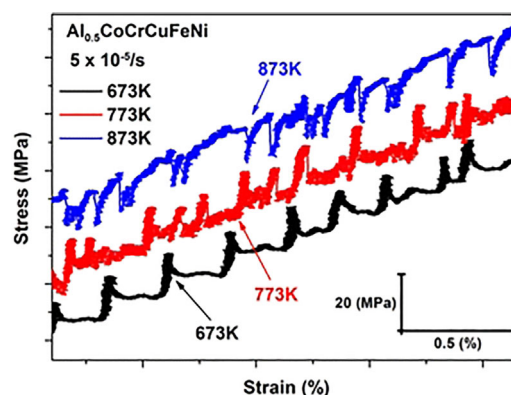

Figure 10. The magnified part of stress–strain curve at different temperatures illustrating upward and downward serrations in $Al_{0.5}$CrFeCoNiCu HEA. Reprinted from ref.[169] with permission from Springer.

heat treatments. The processing route and minor modification to alloy composition have a significant effect on microstructural stability which in turn influence the age hardening behavior and high-temperature properties. It is evident that with proper alloy design and processing route, alloy with enhanced high-temperature properties can be fabricated and applied for high-temperature applications.

4. CrMnFeCoNi

CrMnFeCoNi alloy, also known as Cantor alloy, is one of the most widely studied HEAs and was first reported by Cantor et al.[9] The alloy consists of single FCC phase solid solution in as-cast condition, FCC + secondary phases after heat treatment at intermediate temperatures, and single FCC phase at high temperatures.[15,30,132,175,176] The alloy exhibits unusual work hardening ability, high ductility, and remarkable fracture toughness at room temperature and cryogenic temperature.[57,177–180] The alloy shows increase in yield strength, ultimate strength, and elongation to fracture with decreasing temperature. The enhanced mechanical properties at cryogenic temperature are mainly attributed to the activation of additional deformation mechanism by mechanical nano-twinning.[57,124,181] At high temperatures, this alloy shows the strong temperature dependence of yield strength, serrations in stress–strain curve at intermediate temperatures, and a decrease in work hardening capability with increasing temperature.[177,178,182,183]

Though the alloy has a very high fracture toughness, its yield strength is relatively low at room temperature. Several attempts have been made to improve its yield strength by the addition of carbon, producing fine recrystallized microstructure by thermomechanical processing, and modification of chemical composition by producing non-equiatomic compositions.[178,184–186] Varying the content of Co (x = 5, 10, and 20 at%) or V is reported to influence the mechanical properties of CrMnFeCoNi alloy by promoting the formation of sigma phase.[16,187] The polymorphic transition from FCC to HCP was observed in Cantor alloy using in-situ high-pressure synchrotron radiation XRD technique.[188,189] It has been reported that the stable phase of CrMnFeCoNi alloy at low temperatures and high pressures is HCP phase, whereas the FCC phase is stable at higher temperatures and low pressures. The coexistence of FCC and HCP phases occurs in the pressure range of ≈22 to ≈41 GPa. The critical temperature for the phase transformation from HCP to FCC phase increases with increasing temperature. Moon et al.[190] investigated the deformation induced transformation in a variant of Cr–Mn–Fe–Co–Ni system with low stacking fault energy. They predicted the stable phase at low temperatures as HCP phase using thermodynamic calculations and further verified it experimentally. They observed the formation of HCP phase with an identical composition of FCC phase after cryo-HPT processing of $Cr_{26}Mn_{20}Fe_{20}Co_{20}Ni_{14}$ HEA. They concluded that cryo-HPT process provides an extra driving force for the formation of HCP through deformation induced diffusionless transformation. Bracq et al.[191] investigated the phase stability in Co–Cr–Fe–Mn–Ni system using Calphad and the database (TCHEA1) devoted for HEA. They demonstrated that Cr and Mn destabilize the FCC solid solution and also concluded that the

database accurately describes the FCC phase solid solution, but the σ phase is experimentally observed to be more stable than the predictions. The melting temperature and shear modulus of Cantor alloy are ≈1340 °C[125,192] and 56 GPa,[193,194] respectively.

The major drawback of Cantor alloy is the formation of oxide inclusions during casting and when annealed at high temperatures.[83,194] This can adversely affect the mechanical properties.[184,194] Since Mn has a high vapor pressure, the careful practice of melting should be ensured to minimize the evaporation during melting. In practice, an additional quantity of Mn is added to counteract the loss of Mn.[178,195]

4.1. Precipitation at Intermediate Temperatures

Based on the initial studies on annealing and homogenization of CrMnFeCoNi, the alloy was assumed to retain its single FCC solid solution throughout the temperature range until the onset of melting.[15,43,132,148,177,196] The initial phase stability studies were performed above 800 °C, and the alloy was established to be stable throughout the temperature up to its melting point. For instance, it is demonstrated that the alloy consists of single FCC phase even after annealing at 900 °C for 30 days, 1000 °C for 3 days, and 1100 °C for 1 and 6 h.[15,125,148] However, the recent studies have indicated the formation of the secondary phases at intermediate temperatures below 800 °C after prolonged exposure or straining the material before annealing.[30,31,132,175,197,198]

Schuh et al.[30] were the first one to report the formation of secondary phases at intermediate temperatures. They investigated the thermal stability of the NC CrMnFeCoNi HEA produced by severe plastic deformation. The isochronal annealing of the HPT CrMnFeCoNi HEA alloy with an initial grain size of ≈50 nm resulted in the formation of secondary phases. The 3D-APT analysis (shown in **Figure 11**) revealed the formation of Mn–Ni rich and Cr-rich phases within 5 min of annealing at 450 °C, and an additional phase of Fe and Co was observed after 15 h of annealing. Interestingly, single FCC phase with a substantial increase in grain size of ≈10 μm was observed when annealed at 800 °C for 1 h. The isochronal annealing of the HPT CrMnFeCoNi HEA alloy for 1 h resulted in an increase in hardness with a maximum hardness of ≈630 HV at 450 °C before the hardness starts to decrease. When isothermal annealing was carried out at 450 °C, an increase in hardness was observed with a maximum hardness of ≈910 HV after 100 h before the hardness starts to decrease. The increase in hardness in the intermediate temperature is attributed to the formation of multiphase embedded in the FCC matrix.[30] Maier-Kiener et al.[199] demonstrated the usage of nanoindentation technique to detect phase decomposition in NC CrMnFeCoNi HEA at intermediate temperatures. They observed that Young's modulus increases in the intermediate temperature range and then decreases at high temperature. The Young's modulus is substantially influenced by the secondary phase, but not affected by the grain size. They concluded that nanoindentation could be used as a complementary screening tool for evaluating phase stability of NC HEA in short time. In another study, Lee et al.[200] investigated the annealing effect on plastic flow in nanocrystalline Cantor alloy by nanoindentation studies. They reported the plastic deformation assists the dissolution of annealing-induced
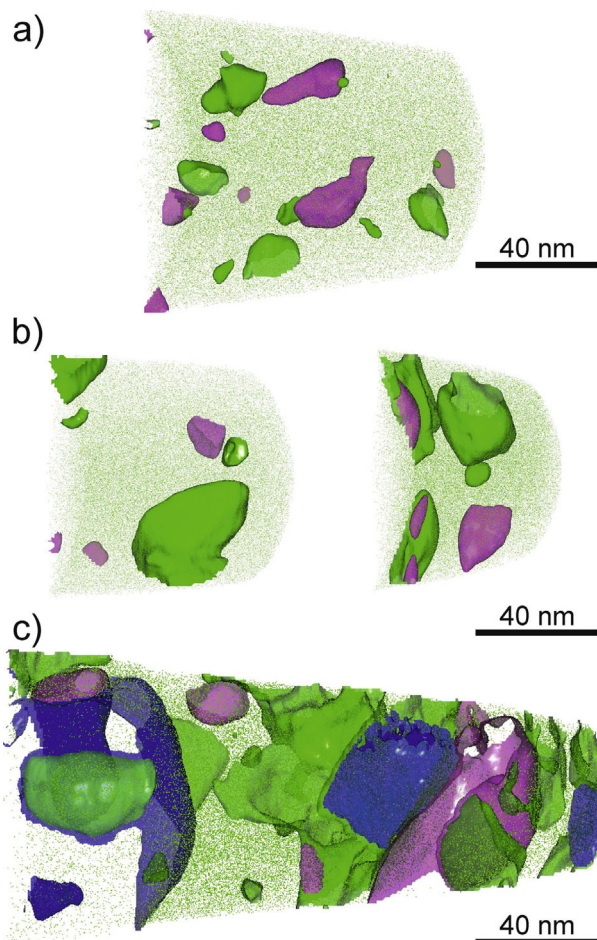
**ADVANCED
SCIENCE NEWS**

www.advancedsciencenews.com

**ADVANCED
ENGINEERING
MATERIALS**

www.aem-journal.com

Figure 11. 3D-APT analysis of SPD CrMnFeCoNi HEA subjected to annealing treatment at 450 °C for the different duration a) 5 min, b) 1 h, c) 15 h. [Green: >70 at% Ni + Mn, Purple: >50 at% Cr, and Blue: >35 at% Co].[30] Reproduced under the terms of the CC-BY-X license.[30]

phase or compound was observed in the microcrystalline alloy (grain size ≈25 μm) even after tensile testing at 500 °C for 20 h.[183] The decomposition of phases occurs within minutes of annealing in the NC material,[30] whereas the decomposition occurs after the long duration of annealing in the microcrystalline material.[31,132,175,199] The difference in kinetics of phase decomposition between coarse grain and NC HEA is attributed to the enhanced diffusion of the NC material because of a lot of grain boundaries. Zhou et al.[197] systematically investigated the precipitation behavior of cold rolled CrMnFeCoNi HEA during annealing at the intermediate temperatures. They observed the precipitation occurred during annealing of cold rolled alloy, but not in non-deformed alloy for the comparable annealing conditions. The Cr-rich precipitates were observed in both recovered and recrystallized samples. They observed a strong correlation between the precipitates and dislocations, and concluded that severe deformation act as a critical factor for the phase decomposition, but not the grain boundaries as suggested by Schuh et al.[30] It is worth mentioning that composition-decomposition is also reported for CoCrFeNi alloy at intermediate temperatures.[151]

Otto et al.[31] investigated the phase decomposition after prolonged annealing at intermediate temperatures and to form the equilibrium phases. The alloy was exposed to different temperatures in the range of 500–900 °C for a long duration of 500 days and the microstructural evolution were characterized by SEM, TEM, and APT. They demonstrated that the alloy consists of single FCC phase after homogenization for 2 days at 1200 °C followed by subsequent annealing at 900 °C for 500 days. The Cr-rich σ phase with tetragonal structure forms primarily along the grain boundaries after annealing at 700 °C for 500 days, and three distinct phases (Cr-rich BCC phase, Ni–Mn rich tetragonal phase, Fe–Co rich ordered B2 phase) form after annealing at 500 °C for 500 days. They concluded that stability of HEAs should be carefully evaluated before considering it for elevated temperature applications.

intermetallic precipitates leading to the considerable strain softening in NC HEA. Park et al.[198] compared the experimental observation and thermodynamic calculation of σ phase formation. They verified the formation of σ phase by thermodynamic calculations based on the TCFE database and concluded that thermodynamic calculations based on TCFE database are suitable for phase predictions in CrMnFeCoNi alloy.

Two different precipitates (carbide and σ phase) were observed in coarse grain HEA during heat treatment at 700 °C for a prolonged duration of 125–1000 h.[132] The formation of carbide is reported at all the heat treated samples, and it is attributed to the contamination of the melting equipment and the starting elements. The σ phase is reported to form after prolonged exposure at 700 °C for 500 and 1000 h, with the increase in volume fraction with heat treatment time. Similarly, the thermomechanical processing by room temperature rolling or cryogenic rolling and subsequent annealing in the temperature range of 600–900 °C for 60 min led to the formation of Cr-rich σ phase and Cr-rich BCC phase.[175] The effect of rolling at room temperature and the cryogenic temperature is insignificant in the secondary phase formation. In another study, no secondary

4.2. Recrystallization and Grain Growth

Bhattacharjee et al.[195] investigated the microstructure evolution during annealing of cold rolled CrMnFeCoNi HEA. The alloy exhibited high recrystallization temperature and strong resistance to grain growth during annealing as compared to TWIP steels. They observed the mechanism for the evolution of recrystallization texture in this alloy is similar to those of TWIP and 316 stainless steel, but notable differences existed due to profuse annealing twin formation.[195,201] Liu et al.[202] investigated the grain growth behavior of 70% cold rolled alloy in the temperature range of 850–950 °C for different durations. They estimated the activation energy of grain growth to be ≈321 kJ mol^{-1} and observed the grain growth kinetics follow a power law with the grain growth exponent of ≈3. The hardness dependence on grain size follows the classical Hall–Petch relationship with a high grain boundary hardening efficient of ≈677 MPa μm$^{-0.5}$ (**Figure 12**). Wu et al.[203] demonstrated that the hardening by grain refinement is more effective in BCC metals and the high Hall–Petch coefficient are generally observed in the BCC than FCC and HCP materials. They
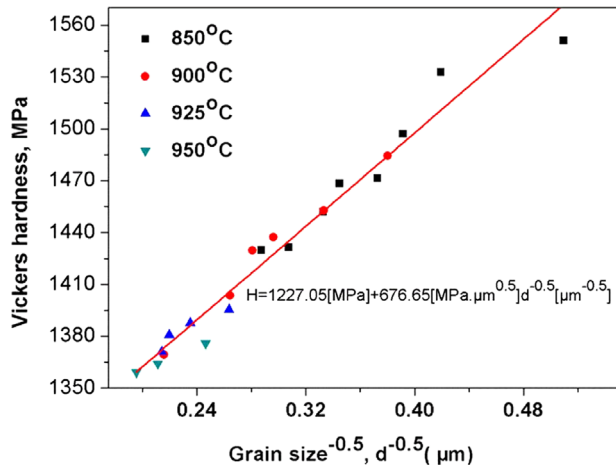
Figure 12. Hardness dependence on the grain size of CrMnFeCoNi HEA illustrating Hall-Petch relationship. Reprinted from ref.[202] with permission from Elsevier.

Figure 13. Hardness variation after heat treatment for 1h at various temperature for samples subjected to different rolling reductions. Reprinted from ref.[204] with permission from Elsevier.

reported that the Hall–Petch coefficient for many FCC metals is not more than $\approx 600\,\text{MPa}\,\mu\text{m}^{-0.5}$. The high Hall–Petch coefficient observed in CrMnFeCoNi alloy gives clear evidence that dislocation motion is difficult in CrMnFeCoNi HEA than conventional alloys.

Otto et al.[204] investigated the recrystallization behavior by subjecting the alloy to different rolling reductions and subsequent annealing in the temperature range of 400–1000 °C. They observed the minimum annealing temperature for complete recrystallization was 800 °C for alloys which underwent rolling reduction above 80%, whereas higher annealing temperature was required for complete recrystallization in alloys with 60% rolling reduction. A noticeable increase in hardness of 10–18% was observed in the temperature range of 400–500 °C as shown in **Figure 13**, which is well below the recrystallization temperature. The influence of rolling reduction above 60% on the grain growth is almost negligible for samples annealed at 800 °C, whereas variation in grain size was observed for higher temperatures and lower rolling reductions. They have carried out the grain growth studies on the recrystallized sample of the 96% cold rolled alloy. The activation energy of $\approx 325\,\text{kJ}\,\text{mol}^{-1}$ and the grain growth exponent of ≈ 3 were estimated in the temperature range of 800–950 °C, similar to the grain growth behavior observed by Liu et al.[202] A rapid decrease in hardness was observed above 600 °C due to recrystallization and grain growth. Even though no apparent recrystallization occurred in the temperature range of 400–500 °C, the reason for the increase in hardness at this temperature range remained an open question in that study. However, the recent literature findings suggest that the formation of the secondary phases in that temperature range could be a possible reason for the increase in hardness. Otto et al.[204] investigated the twin formation in CrMnFeCoNi after thermomechanical processing. They observed the twin fractions tends to increase with increasing thickness reduction for samples annealed at 800–1000 °C. The increase in twin fraction with rolling thickness is significant at high temperatures. For rolling reduction above 84% and annealing at 1000 °C, the twin fraction accounts for $\approx 57\%$ of internal boundaries. They
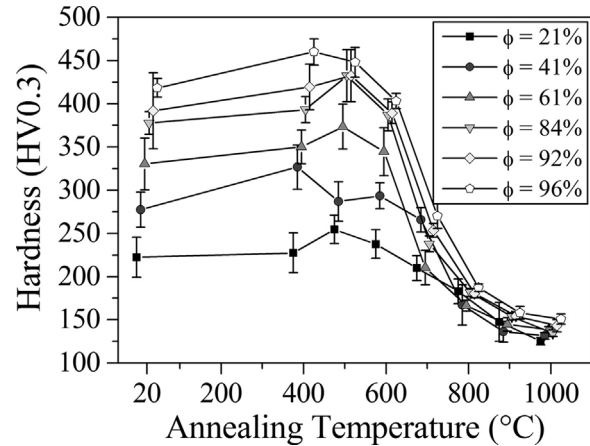
concluded that the formation of twins during grain growth in a fully recrystallized material is determined by the final grain size and independent of the heat treatment required to achieve that grain size.

Stepanov et al.[185] doped the Cantor alloy with 1 at% of C and investigated the effect of thermomechanical processing on microstructure and mechanical properties. They observed the complete recrystallization of 80% cold rolled sample occurs in the temperature range of 700–1100 °C. The alloy showed a decrease in yield strength and increase in ductility with an increase in annealing temperature. The good combination of mechanical properties was achieved after annealing at 800 °C. The alloy exhibited yield strength of 720 MPa, ultimate tensile strength of 980 MPa, and elongation to fracture of 37% after annealing at 800 °C. For a similar grain size, the carbon doped alloy has twice higher yield strength, 50% higher ultimate tensile strength, and with almost similar ductility as carbon-free CrMnFeCoNi alloy.

4.3. Mechanical Behavior at Elevated Temperatures

The Cantor alloy shows the strong temperature dependence of yield strength, serrations in stress–strain curve at intermediate temperatures, and complex behavior of elongation to fracture with increasing temperature.[178,183] The average grain size of CrMnFeCoNi alloy after cold rolling (87% reduction) followed by annealing at 800, 1000, and 1150 °C for 1 h are 4.4, 50, and 155 μm, respectively.[178] The alloy with fine grain size exhibited high yield strength from room temperature up to 600 °C as compared to coarse grain size. Above 600 °C, the yield strength dropped significantly ($\approx 50\%$ drop) for fine grain size while the drop was not significant in the coarse grain size material.[178] The alloy exhibited the contrasting behavior of elongation to failure between fine grain size and coarse grain size. For instance, a decrease in ductility with an increase in temperature was observed for coarse grain size, whereas the ductility decreased from RT to 400 °C and above which the ductility increased

for fine grain size. Also, the yield point was observed in fine grain size at lower temperatures ($<400\,°C$), but not at higher temperatures. Pronounced serrations were observed in the stress–strain curve at $400\,°C$ for both fine and coarse grain sizes. From room temperature till $600\,°C$, the initial plastic deformation till 2% strain occurred by planar glide; and at higher strains, the slip becomes more homogeneous leading to the formation of cell structures. Hong et al.[205] attributed the transition of dislocation structure from planar to cell structure are mainly due to the shearing of nanoscale inhomogeneity with strain.

Woo et al.[206] investigated the high-temperature deformation behavior by studying the evolution of mesoscopic lattice behavior using in-situ neutron diffraction. In situ neutron diffraction and TEM experiments revealed that dislocation glide and diffusion-controlled dislocation creep act as dominant deformation mechanism at 527 and $727\,°C$, respectively. The mesoscopic lattice behaviors, such as lattice strain, integrated intensity, and peak width observed at RT and $527\,°C$, were similar to those of the conventional single-phase FCC alloys at RT and elevated temperatures. Reddy et al.[207] demonstrated the superplasticity behavior in fine-grained CrMnFeCoNi alloy. The alloy, when studied at $750\,°C$ and over a range of strain rates from 10^{-4} to $10^{-1}\,s^{-1}$, showed superplastic flow like behavior with an elongation to failure of $\approx320\%$ at a strain rate of $10^{-4}\,s^{-1}$ (**Figure 14**). The alloy exhibited strain hardening and texture weakening at low strain rate, whereas flow softening and texture strengthening were observed at high strain rate. They suggested the possible deformation mechanism as superplasticity by grain boundary sliding based on the data extracted from the cyclic strain rate test. They observed the deformation-enhanced grain growth in alloy with a grain size of $\approx1.4\,\mu m$ when tested at 1023 K and $10^{-4}\,s^{-1}$ strain rate, which further confirmed the superplasticity by grain boundary sliding mechanism. Besides, static grain growth was observed when tested at 1023 K and at $10^{-1}\,s^{-1}$, which implies that diffusion in HEAs may not be sluggish at high temperatures. Eleti et al.[208] systematically investigated the hot deformation behavior of CrMnFeCoNi HEA by conducting hot compression tests in the temperature range of

800–1000 °C and at various strain rates (10^{-3}–$1\,s^{-1}$). They reported that the apparent activation energy for hot deformation was estimated to be $\approx350\,kJ\,mol^{-1}$, which is similar to the diffusion activation energy of Ni in this alloy.

Another striking feature of this alloy is the observation of high strain hardening and serrations in the stress–strain curve in the intermediate temperature range of 300–600 °C (shown in **Figure 15**).[183] The decrease in critical strain for the onset of serrations and the evolution of serrations from type A to A + B and then to type B and B + C are observed with increasing temperature and decreasing strain rate. In the temperature range of 300–500 °C, the dislocation pinning by solute was controlled by pipe diffusion with an apparent activation energy of $\approx116\,kJ\,mol^{-1}$, whereas cooperative lattice diffusion with an apparent activation energy of $296\,kJ\,mol^{-1}$ dominated the pinning process at 500–600 °C. The TEM analysis of the deformed sample at a low plastic strain of $\approx1\%$ reveals the low density of dislocations at RT and $400\,°C$ and high density of dislocations piled up at grain boundaries at $600\,°C$. However, at the high plastic deformation of $\approx20\%$ strain, high density of dislocations and dislocation cell structure were observed at RT and $400\,°C$, whereas the low density of dislocations with kinking and bowing of dislocations was observed at $600\,°C$. The lower dislocation density at $600\,°C$ is attributed to the thermal recovery, and the observation of kinks and bowing of dislocation is attributed to the pinning process by solute atoms.

5. Refractory High-Entropy Alloys

Senkov et al.[209] attempted to produce HEAs based on refractory elements with superior high-temperature properties over superalloys for high-temperature applications. The NbMoTaW and VNbMoTaW refractory HEAs exhibited single BCC phase, very high hardness, and very high yield strength at elevated temperatures.[74,209] For instance, the alloys showed high yield strength in the range of 400–500 MPa at 1600 °C. The variation of the yield strength of various refractory HEAs at different temperature are shown in **Figure 16**, and it is evident that refractory HEAs have exceptional resistance to softening at elevated temperatures as compared to those of conventional
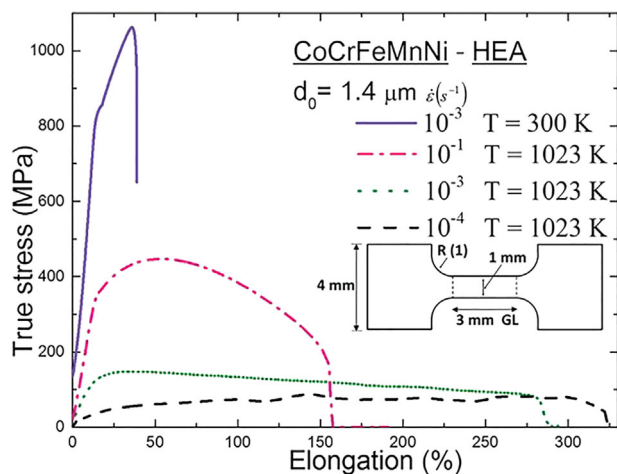

Figure 14. Superplastic like flow behavior in CrMnFeCoNi HEA at high temperatures.[207] Reproduced under the terms of the CC-By-X license.[207]
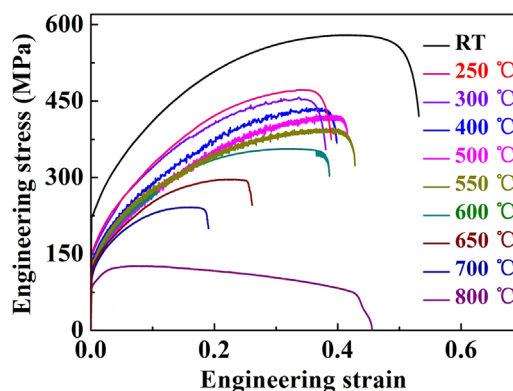

Figure 15. Engineering stress–strain curves at different temperature for CrMnFeCoNi HEAs. Reprinted from ref.[183] with permission from Elsevier.
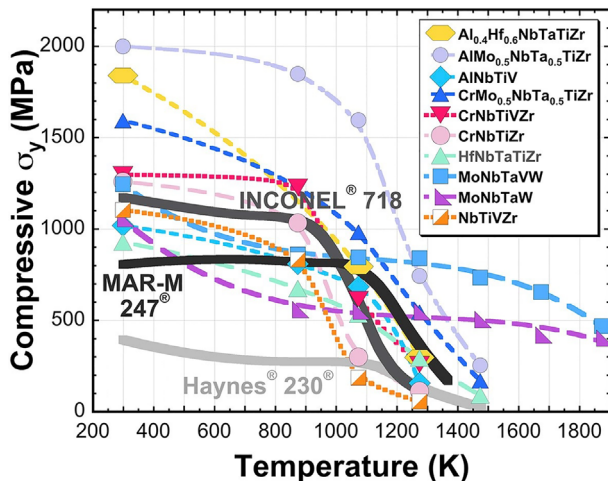
Figure 16. Yield strength variation of refractory HEAs illustrating superior strength retention at a higher temperature than superalloys.[6] Reproduced under the terms of CC-BY-X license.[6]

superalloys. However, the density of refractory HEAs are very high (13.8 g cm^{-3} for NbMoTaW, and 12.4 g cm^{-3} for VNbMoTaW) and the alloy exhibits a poor elongation to fracture at room temperature. To decrease the density and to improve the room temperature ductility, the high-density elements are replaced by low-density elements. The HfNbTaTiZr HEA (density $\approx$9.94 g cm^{-3}) possess superior room temperature mechanical properties with high compression yield strength of 929 MPa, homogeneous macroscopic flow, and ductility greater than 50%.[210] However, the alloy has a meager yield strength of $\approx$92 MPa at 1200 °C.[134] In order to enhance the high-temperature strength and further reduce the density of HfNbTaTiZr, several attempts have been made by adding low-density elements like Mo, Cr, Ti, and Al [133,211] or by adding Si so that it forms a low-density secondary phase.[212] The addition of Mo to HfNbTaTiZr increased the compressive yield strength from $\approx$100 to $\approx$550 MPa at 1200 °C and exhibited reasonable RT ductility of 12%.[136] The compressive stress–strain curve of MoNbHfZrTi alloy showed strain hardening stage until fracture at 800 °C and strain rates of 10^{-1}–10^{-2} s^{-1}, whereas DRX characteristics were observed at a temperature over 800 °C and at strain rates of 10^{-3}–10^{-1} s^{-1}. The alloy showed a decrease in strength and the occurrence of DRX with increasing temperature and decreasing strain rate. Discontinuous and continuous DRXs occurred simultaneously, with reduced effect of CDRX at high deformation temperature and low strain rate.[137]

The partial substitution of Al with Hf in HfNbTaTiZr reduced the density by 9% and increased the room temperature yield strength by 98%, but the room temperature ductility reduced to 10% with no significant enhancement in the high-temperature strength.[211] The addition of Mo in place of Hf and reducing the Ta content to half have resulted in the increase of high-temperature strength from $\approx$90 to 250 MPa at 1200 °C with a perceptible increase in RT ductility in AlMo$_{0.5}$NbTa$_{0.5}$TiZr HEA.[211] THe HfMo$_{0.5}$NbTiV$_{0.5}$ HEA forms a single BCC phase, and the addition of Si led to the formation of multi-component silicide.[212] The yield strength increased from 1260 to 2134 MPa with the addition of Si, but with the reduction in ductility from >35 to 9.2%. The Si

addition to HfMo$_{0.5}$NbTiV$_{0.5}$ alloy has shown a remarkable effect on the yield strength at elevated temperatures. The yield strength of the alloy at 1200 °C increased from 60 to 166, 188, and 235 MPa for the silicon addition of 0.3, 0.5, and 0.7-mole fraction, respectively.[212] The addition of Si to AlTiCrNbMo refractory HEA resulted in a slight increase in the oxidation resistance.[54] The oxidation behavior of AlTiCrNbMo HEA showed the formation of porous and non-protective oxides scales, and the oxidation kinetics followed the linear rate law at 900 and 1000 °C. The addition of Si reduced the mass gain and formed a thin and compact oxide scale as compared to the Si-free alloy.

The grain growth kinetics study on HfNbTaTiZr alloy at 1200–1350 °C reveals a high activation energy of $\approx$389 kJ mol^{-1} and growth exponent of $\approx$3.5.[138] The activation energy is comparable to the activation energy of Nb (397 kJ mol^{-1}) and Ta (413 kJ mol^{-1}), which indicates that Nb and Ta control the grain growth rate in this alloy. Interestingly, the Hall-Petch coefficient (240 MPa µm^{-2}) of this alloy is significantly lower than the CrMnFeCoNi ($\approx$670 MPa µm^{-2}) alloy. The reduction in grain size from 128 to 38 µm has enhanced the fracture strain from 15 to 20% with a perceptible increase in yield strength from $\approx$940 to $\approx$960 MPa.

Zou et al.[101] fabricated a refractory NC columnar NbMoTaW HEA and demonstrated the strength retention up to 600 °C. The yield strength of NC HEA decreased from 7 GPa at room temperature to 5 GPa at 600 °C, while the single crystal HEA decreased from 2 GPa at room temperature to 1 GPa at 600 °C . The NC HEA showed strength reduction of only 20% while the strength reduction in coarse grain HEA is 50%. The NC HEA exhibited higher normalized strength and specific strength in a wide range of temperature. At the same homologous temperature, the compressive property of NC HEA has outperformed most of the other NC metals, superalloys, coarse grain HEAs. The enhanced microstructural stability is attributed to the presence of nanoscale nitrides and oxides at the grain boundaries, due to contamination from raw materials. The other reason could be the low thermodynamic driving force for grain boundary motion due to highly chemically disordered structures in both grain interior and grain boundaries. Even though refractory HEAs have superior high-temperature mechanical properties, the practical application of refractory alloys is hindered by high raw material cost, high density, poor ductility at room temperature, and poor oxidation behavior.[48,83,213,214]

6. High-Temperature Properties of Other HEAs

Mohanty et al.[215] studied the aging behavior of AlCoNiCuZn HEA synthesized by mechanical alloying (MA) with subsequent spark plasma sintering (SPS). The sintered alloy was solutionized at 1160 °C for 96 h followed by quenching in cold water. The isothermal and isochronal aging treatments were carried out followed by ice water quenching. The peak hardness was observed at 500 °C, and the hardness increased from $\approx$1.6 GPa in the solutionized state to 6 GPa after age hardening at 500 °C. The increase in hardness was attributed to the precipitation of ordered FCC precipitates in the FCC matrix.[215]

He et al.[83] tweaked the alloy design and successfully produced CrFeCoNi alloy with a fine dispersion of nano-sized

coherent precipitates by the addition of 2 at% Ti and 4 at% Al. The steady stress in CrFeCoNi with coherent precipitates is 117 MPa at 850 °C and a strain rate of $6.410 \times 10^{-6}\,s^{-1}$. However, the steady stress achieved in a single FCC phase CrMnFeCoNi HEA at the same temperature and strain rate is significantly lower ≈ 33 MPa.[194] At the stress of 110 MPa, the strain rate achieved in $(CrFeCoNi)_{94}Ti_2Al_4$ alloy was in the order of $\approx 10^{-5}$, which is two order magnitude lower than that of the single-phase CrMnFeCoNi alloy ($\approx 10^{-3}$) (shown in **Figure 17**).[83]

The dissolution of coherent precipitates above 850 °C led to distinct deformation behavior regimes: Regime I: 750–850 °C, Regime II: 875–900 °C. The high-stress exponent of 6–9 and high activation energy of 600 kJ mol^{-1} at temperatures below 850 °C and stress exponent of ≈ 5 and activation energy between 350–450 KJ mol^{-1} above 875 °C indicates threshold stress effect and dislocation climb, respectively. Unlike CrMnFeCoNi alloy, the microstructural deterioration such as Mn oxide and Cr –rich secondary phases are not observed in this alloy.

Wang et al.[216] investigated the effect of high melting element, Mo, on the high-temperature compressive deformation behavior of CrFeCoNiMo$_{0.2}$ HEA prepared by gas atomization and SPS. It is reported that the DRX act as the dominant softening mechanism in the temperature range of 800–1100 °C. The formation of Mo-rich σ phase prevents grain coarsening during DRX and results in the formation of fine grain size. The alloy is reported to have a very high deformation activation energy of ≈ 463 kJ mol^{-1}, which is comparable to the activation energy of superalloys and significantly higher than other HEAs: Al$_{0.5}$CrFeCoNi (≈ 300 kJ mol^{-1}), AlCrFeCoNiCu (≈ 306 kJ mol^{-1}), and CrMnFeCoNi HEAs (≈ 291 kJ mol^{-1}).[168,217,218] Samal et al.[174] investigated the hot deformation behavior of TiFeCoCuNi eutectic HEA and suggested the optimum hot working temperature in the range of 930–990 °C and strain rate in the range of $10^{-3}\,s^{-1}$–$10^{-1}\,s^{-1}$. They observed that the amplitude of serrations in flow curve increased with decreasing temperature at high strain rate and suggested that the presence of multi-substitutional solute atoms as a possible reason for the occurrence of serrations.
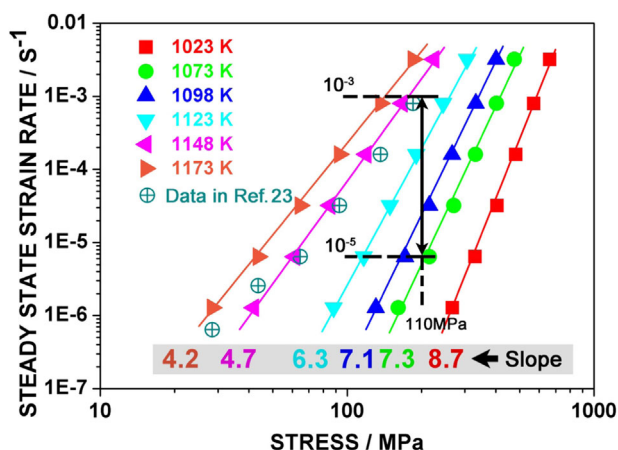
Tsau et al.[219] investigated the annealing effect on phase transformation and mechanical behavior in CoFeNiTi alloy and reported that CoFeNiTi consisted of ordered HCP dendrites and FCC inter-dendrites in the as-cast condition. They observed that the heat treatment at 1000 °C did not affect the ordered HCP dendrites, but the ordered FCC has transformed to disordered FCC phase. They observed the better compressive properties when the sample was annealed at 1000 °C for 24 h. They concluded that the high ultimate tensile strength after annealing was mainly due to the disordering of FCC phase which can sustain more deformation than the ordered structure. Xian et al.[220] developed a new V$_{35}$Ti$_{33}$Fe$_{15}$Cr$_{10}$Zr$_5$ HEA with single BCC phase for fusion reactors in the temperature range of 25–900 °C. The yield strength of the alloy increased with increasing temperature below 500 °C, but with a reduced ductility. The alloy showed reasonable ductility of >12% above 700 °C with a yield strength of ≈ 800 MPa at 700 °C, which is 500 MPa higher than that of candidate alloys for a fusion reactor. Manzoni et al.[221] attempted to optimize an HEA based on Al–Ti–Cr–Fe–Co–Ni–Cu system for high-temperature applications. They concluded that the Al$_{10}$Ti$_6$Cr$_8$Fe$_{15}$Co$_{25}$Ni$_{36}$ HEA possess enhanced ultimate tensile strength up to ≈ 800 °C and it is superior over commercial superalloys. Sathiyamoorthi et al. demonstrated a remarkable thermal stability in CrFeCoNi HEA synthesized by MA and SPS.[102,222] They observed an exceptional resistance to anneal softening at the temperature range of 700–900 °C for a prolonged duration of 600 h. It is reported that the fractional decrease in hardness and the increase in grain size after annealing at 700 °C for 600 h are negligible. They attributed the remarkable thermal stability of this alloy to the composite microstructure achieved after sintering due to the contamination during synthesis. The unpublished work by Praveen and Kottada on compression creep behavior of CrFeCoNi HEA, as reported in a recent overview article by Chokshi,[103] is the only work on conventional creep behavior of HEAs in the literature. They observed an effective stress exponent of ≈ 5 and effective activation energy of ≈ 365 kJ mol^{-1} based on the threshold stress approach. However, the alternative approach by Chokshi[103] based on Sherby–Burke criterion reveals a power-law breakdown in the experimental data obtained by Praveen and Kottada for CrFeCoNi and He et al. for CrMnFeCoNi HEAs (shown in **Figure 18**).

6.1. High-Temperature Oxidation and Hot Corrosion Resistance

Tsao et al.[223] investigated the high-temperature oxidation and corrosion properties of high-entropy superalloys based on Al–Ti–Cr–Fe–Co–Ni system and compared their properties with CM247LC – Ni-base superalloy. The oxidation tests were performed in the temperature range of 900–1100 °C for the duration of 5–200 h. They studied the corrosion behavior by performing the salt-coated and crucible tests. They observed that high entropy superalloys form complex oxides due to various solutes, and concluded that the high content of Cr and Al promotes the formation of protective chromia and alumina layers. They demonstrated an excellent hot corrosion and oxidation resistance in alloys which form Cr$_2$O$_3$ and Al$_2$O$_3$ scales, respectively. Dogan et al.[224] investigated the elevated temperature corrosion of B$_x$Al$_{0.5}$CrFeCoNiCu HEAs in the

Figure 17. Stress variation as a function of strain rate and temperature in double logarithmic axis with different stress exponents. The result of CrMnFeCoNi is also plotted for direct comparison with $(CrFeCoNi)_{94}Ti_2Al_4$ alloy. Reprinted from ref.[83] with permission from Elsevier.

**ADVANCED
SCIENCE NEWS**

www.advancedsciencenews.com

**ADVANCED
ENGINEERING
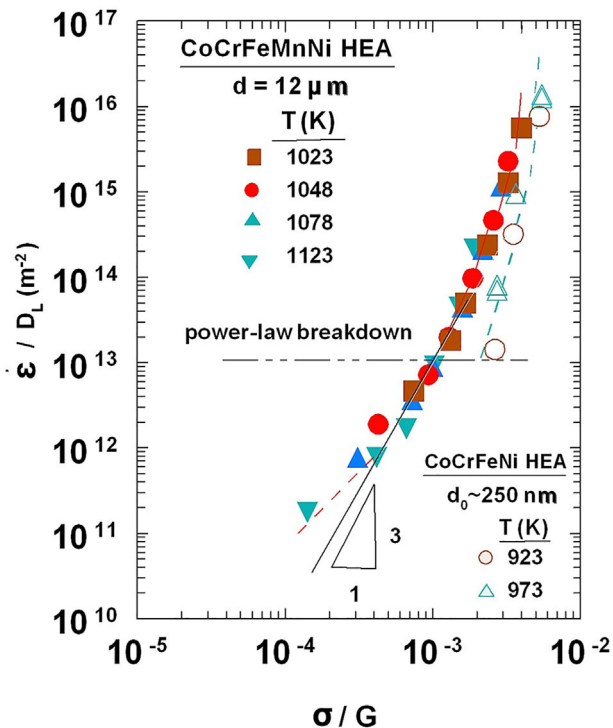MATERIALS**

www.aem-journal.com

Figure 18. Transition of deformation mechanism from power-law intragranular dislocation creep to a power-law breakdown regime in CrMnFeCoNi and CrFeCoNi HEAs. Reprinted from ref.[103] with permission from Elsevier.

simulated syngas at 500 °C. They reported the corrosion of HEAs at 500 °C is negligible in syngas containing 0 and 0.01% H_2S, whereas a significant corrosion was observed in syngas containing 0.1 and 1 % H_2S. The formation of Fe–Cr-borides with the increase in B content reduced the corrosion resistance of these alloys.

Bulter et al.[225] investigated the oxidation behavior of $Al_{10}Cr_{22.5}Fe_{22.5}Ni_{22.5}Co_{22.5}$ (Al10) and $Al_{20}Cr_{25}Ni_{25}Co_{25}Si_5$ (Al20-S) HEAs at 1050 °C in dry air. They observed the formation of discontinuous external Cr_2O_3 with internal Al_2O_3 subscale and AlN precipitates in the former alloy and a continuous external layer of Al_2O_3 scales with a small volume fraction of Cr_2O_3 in the later alloy. The formation of a continuous external layer of Al_2O_3 resulted in better oxidation resistance in the Al20-S HEA than the Al10 HEA. They concluded that long-term oxidation behavior of these alloys depends on the Al and/or Cr contents in the subsurface and the depth of elemental depletion due to the oxide scale formation. Jiang et al.[226] investigated the oxidation behavior of AlTiCrFeNiCo HEA at 850 °C in the air. They observed the oxidation kinetics follow parabolic rate law. Butler and Weaver investigated the oxidation behavior of series of arc-melted $Al_x(CrFeCoNi)_{100-x}$ HEAs at 1050 °C. They observed the various degrees of parabolic oxide growth and the formation of external Cr_2O_3 scale with an internal Al_2O_3 and AlN scales in all the HEAs. They concluded that the increase in Al content enhances the oxidation resistance by forming continuous internal Al_2O_3 oxidation layer. Kai et al.[227] investigated the oxidation behavior of SiCrFeCoNi,

CrMnFeCoNi, and AlCrFeCoNi HEAs in dry air at 700–900 °C. They observed all the three alloys follow parabolic rate law in the studied temperature range, with the oxidation rates of AlCrFeCoNi < SiCrFeCoNi < CrMnFeCoNi. The better oxidation resistance in AlCrFeCoNi HEA as compared to SiCrFeCoNi and CrMnFeCoNi is attributed to the formation of the Al_2O_3 oxide layer. Dabrowa et al.[228] investigated the influence of Cu content on the high-temperature oxidation behavior of $AlCrFeCoNiCu_x$ HEAs at 1000 °C for the duration of 100–500 h. They observed a decrease in oxidation resistance and adhesion of Al_2O_3 oxide layer with the increase in Cu content.

Laplance et al.[229] investigated the oxidation behavior of CrMnFeCoNi HEA in the temperature range of 500–900 °C for the time duration of 100 h in the laboratory air. They observed the oxidation rate was linear at the initial duration and became parabolic at longer times. The alloy exhibited a strong temperature dependence of oxide scale formation: Mn_2O_3 at 600 °C, Mn_2O_3 with Cr enrichment at 700 and 800 °C, and Mn_3O_4 at 900 °C. Kai et al.[230] investigated the oxidation behavior of CrMnFeCoNi at 950 °C in the various oxygen-containing atmosphere with oxygen partial pressure ranging from 10 to 10^5 Pa. The oxidation kinetics followed the parabolic rate law, and the oxidation rate constants increased with increasing oxygen partial pressure. They reported the formation of triplex oxide layer consists of the Mn_3O_4-outer layer, Mn_3O_4, $(Mn, Cr)_3O_4$ – intermediate layer, and Cr_2O_3 – inner layer. Holcomb et al.[231] systematically investigated the oxidation behavior of CrMnFeCoNi family at 650 and 750 °C for 1100 h in laboratory air. They observed the alloys with low Mn content, and high Cr content exhibited better oxidation resistance. The addition of Y is reported to increase the oxidation resistance by improving the adhesion of oxide scales. The alloy without Cr exhibited increased oxidation rates and scale spallation than Cr containing alloys. They reported an excellent oxidation resistance in CrFeCoNi, which is comparable to 304H alloys at 650 °C. Kai et al.[232] investigated the oxidation behavior of FeCoNi, CrFeCoNi, and CrFeCoNiCu HEAs over the temperature range of 800–1000 °C in dry air. They observed the oxidation behavior follows the parabolic rate law and the formation of triplex scales in all the HEAs. The oxidation resistance in the decreasing order is reported to be CrFeCoNi > CrFeCoNiCu > FeCoNi, and the better oxidation resistance in CrFeCoNi HEA is attributed to the formation of Cr_2O_3.

Rao et al.[233] studied the oxidation behavior of $Al_xCr_{0.4}Mn$-$Fe_{0.4}NiCu$ HEAs at 800 °C for the duration of 5–40 h in air. They reported a significant enhancement in the oxidation resistance with the increase in Al content due to the formation of the protective Al_2O_3 layer. The oxidation behavior initially obeyed the parabolic rate law followed by the linear rate for the longer duration. Chen et al.[161] investigated the oxidation behavior of $Al_xCrMnFe_{1.5}Ni_{0.5}$ alloys and demonstrated good oxidation resistance in alloy with higher Al content being better than the lower Al content. They observed the formation of Mn-rich oxide in the external layer and dense protective Cr and Al-rich oxides layer. Chen et al.[234] investigated the oxidation behavior of $AL_{1.3}CrFeNi$ HEA and observed the oxidation kinetics follow parabolic rate law after 5 h. They observed the oxide scale consist of Al_2O_3, Cr_2O_3, and $FeCr_2O_4$

ADVANCED
SCIENCE NEWS
www.advancedsciencenews.com

ADVANCED
ENGINEERING
MATERIALS
www.aem-journal.com

Senkov et al.[48] investigated the oxidation behavior of $TiCrZrNbMo_{0.5}Ta_{0.5}$ refractory HEA at 1000 °C for 1000 h in air and demonstrated better oxidation resistance than commercial Nb alloys. They reported the formation of continuous oxide scale consist of complex oxides, and the oxidation kinetics followed a near-parabolic dependence. Liu et al.[214] developed refractory HEAs with the addition of Cr, Al, and Si to improve the oxidation resistance and demonstrated the enhancement in oxidation resistance with the addition of Ti and Si, and removal of V. They observed the formation of the Al_2O_3 layer at the outermost oxide scales, and the oxidation kinetics followed linear behavior in all refractory HEAs at 1300 °C. Gorr et al.[213] investigated the oxidation behavior of AlTiCrMoW HEA at 1000 °C for 40 h in air atmosphere. They observed a thick oxide scale consists of TiO_2, Al_2O_3, Cr_2O_3, and WO_3 with a discontinuous layer of Cr_2O_3 at the interface. The oxidation rate follows the parabolic rate law with high oxidation rate. They suggested that the addition of Nb may facilitate the formation of continuous Al_2O_3 layer and enhance the oxidation behavior, which is based on the influence of Nb in conventional alloys such as Ti–48Al–2Cr and TiAl alloys.

6.2. Thermal Stability of HEA Coatings

Due to the unique properties of HEAs, the application of HEAs as a potential coating material for high-temperature applications is quite exciting. Hsu et al.[235,236] investigated the $NiCo_{0.6}Fe_{0.2}Cr_{1.5}SiAlTi_{0.2}$ HEA coating processed by SPS and atmospheric plasma spray (APS) and compared the results with MCrAlY. The HEA coatings processed by SPS exhibited a high hot hardness of ≈230 HV at 1100 °C while the hardness of MCrAlY at 1100 °C is ≈55 HV. The high hardness in HEAC is attributed to the dispersion of harder Cr_3Si phase as compared to the dispersion of NiAl in MCrAlY. The HEA coating processed by SPS exhibited 30% lower thermal conductivity than that of MCrAlY at 1000 °C and exhibited oxidation behavior similar to that of MCrAlY at 1100 °C. The HEA coating processed by APS also showed oxidation resistance similar to MCrAlY coatings at 1100 °C due to the formation of a dense thermally grown oxide layer of Al_2O_3 and Cr_2O_3. They concluded that HEA coating processed by SPS and APS have the potential to replace the conventional MCrAlY as overlay coating for high-temperature applications due to their higher hot hardness, good oxidation resistance, low thermal conductivity, and low thermal expansion. Huan et al.[49] demonstrated an enhancement in oxidation resistance of Ti–6Al–4V alloy at 800 °C in the air due to the laser clad coating of AlSiTiVCr HEA. The enhancement in oxidation resistance is attributed to the formation of dense and adherent multi-oxide scale. Zhang et al.[51] demonstrated a remarkable thermal stability of laser cladded CrFeCoNiCu HEA coating on Q235 steel substrate up to 750 °C. Cai et al.[237] investigated the thermal stability of TiVCrCoNi HEA coatings by laser surface alloying on Ti–6Al–4V substrate. They observed the coatings remained stable even after annealing at 900 °C for 8 h, and attributed the oxidation resistance of HEA coating to the formation of NiO and the alloying elements: Al, Cr, and Co. Dolique et al.[238] reported the stability of AlCrFeCoNiCu HEA thin film up to 510 °C using in-situ XRD. Cheng et al.[73,239]

demonstrated a remarkable thermal stability of amorphous structure in $Ge_xTiZrNbTa$ and BTiZrNbTa HEAs thin film after annealing in the temperature range of 700–800 °C for 1 h in a vacuum. They attributed the exceptional thermal stability of amorphous structure to the combination of high entropy, significant atomic size differences, and enhanced sluggish diffusion. Feng et al.[240] demonstrated a very good structural stability in NC NbMoTaW refractory HEA thin film up to 800 °C for 2 h. Tsai et al.[241–243] investigated the diffusion barrier properties of AlSiTiVZrNbMoTa, $(AlSiTiVZrNbMoTa)_{50}N_{50}$, SiTiZrNbTa HEAs film by placing an HEA thin film layer between the Cu and Si. They demonstrated a superior diffusion barrier capability in HEA films which can prevent inter-diffusion and reaction between Cu and Si up to 900 °C. They attributed the higher structural stability and higher chemical stability of HEA films to the low driving force of crystallization, severe lattice strain, and slow diffusion kinetics.

7. Concluding Remarks

This article reviewed the advancement in the field of HEAs regarding its potential as high-temperature materials. It is evident that the outstanding properties of HEAs make them a potential candidate for high-temperature applications. The vast majority of the articles are focused on producing single phase HEAs, and very few studies attempted to produce HEAs with more than one phase. In contrast, the current high-temperature conventional materials such as Ni-base superalloys achieve their superior properties mainly due to the presence of second phase. There is a tremendous scope to explore HEAs with a two-phase microstructure or composite microstructure or dispersion of stable oxides to achieve enhanced high-temperature properties. The present review article reveals that the HEAs are established as a potential candidate for high-temperature application based on the constant strain rate experiments at high temperature and the assumption of diffusivity being sluggish. However, the potential of HEAs as high-temperature material should be mediated based on the creep behavior at elevated temperatures. There are only a few studies on creep behavior,[103] and most of them are studied by nanoindentation technique at room temperature.[244–246] Moreover, the analysis of nanoindentation data requires necessary caution due to relatively low strain achieved in the nanoindentation studies.[103] The conventional creep experiments should be investigated to find out the deformation resistance behavior which would reveal the real potential of HEAs as high-temperature materials. The HEA field is still in its incipient stage and requires profound research on the high-temperature deformation behavior of HEAs. It is possible to design HEAs with superior high-temperature properties over superalloys with the available advanced experimental and modeling techniques.

Acknowledgements

[1] J. R. Davis, *Alloying: Understanding the Basics*, ASM International, USA, **2001**.

[2] S. Ranganathan, *Curr. Sci.* **2003**, *85*, 1404.

[3] M. F. Ashby, K. Johnson, *Materials and Design: The Art and Science of Material Selection in Product Design*, Butterworth-Heinemann, UK, **2013**.

[4] J. W. Yeh, S. K. Chen, S. J. Lin, J. Y. Gan, T. S. Chin, T. T. Shun, C. H. Tsau, S. Y. Chang, *Adv. Eng. Mater.* **2004**, *6*, 299.

[5] B. Murty, J.-W. Yeh, S. Ranganathan, *High-entropy alloys*, Butterworth-Heinemann, UK, **2014**.

[6] D. B. Miracle, O. N. Senkov, *Acta Mater.* **2017**, *122*, 448.

[7] A. L. Greer, *Nature* **1993**, *366*, 303.

[8] H. Baker, H. Okamoto, *Alloy Phase Diagrams* **1992**, *3*, 2.

[9] B. Cantor, I. T. H. Chang, P. Knight, A. J. B. Vincent, *Mater. Sci. Eng. A* **2004**, *375*, 213.

[10] P. K. Huang, J. W. Yeh, T. T. Shun, S. K. Chen, *Adv. Eng. Mater.* **2004**, *6*, 74.

[11] J.-W. Yeh, S.-J. Lin, T.-S. Chin, J.-Y. Gan, S.-K. Chen, T.-T. Shun, C.-H. Tsau, S.-Y. Chou, *Metall. Mater. Trans. A* **2004**, *35*, 2533.

[12] J. W. Yeh, *JOM.* **2013**, *65*, 1759.

[13] Y. Jien-Wei, *Ann. Chim. Sci. Mat.* **2006**, *31*, 633.

[14] J. W. Yeh, *JOM.* **2015**, *67*, 2254.

[15] F. Otto, Y. Yang, H. Bei, E. P. George, *Acta Mater.* **2013**, *61*, 2628.

[16] Z. G. Zhu, K. H. Ma, X. Yang, C. H. Shek, *J. Alloys Compd.* **2017**, *695*, 2945.

[17] O. N. Senkov, J. D. Miller, D. B. Miracle, C. Woodward, *Nat Commun.* **2015**, *6*, 6529.

[18] D. C. Ma, B. Grabowski, F. Kormann, J. Neugebauer, D. Raabe, *Acta Mater.* **2015**, *100*, 90.

[19] N. G. Jones, J. W. Aveson, A. Bhowmik, B. D. Conduit, H. J. Stone, *Intermetallics* **2014**, *54*, 148.

[20] N. G. Jones, A. Frezza, H. J. Stone, *Mater. Sci. Eng. A* **2014**, *615*, 214.

[21] S. Praveen, B. S. Murty, R. S. Kottada, *Mater. Sci. Eng. A* **2012**, *534*, 83.

[22] S. Guo, C. T. Liu, *Prog. Nat. Sci.: Mater. Int.* **2011**, *21*, 433.

[23] Y. P. Wang, B. S. Li, H. Z. Fu, *Adv. Eng. Mater.* **2009**, *11*, 641.

[24] T. T. Shun, C. H. Hung, C. F. Lee, *J. Alloys Compd.* **2010**, *493*, 105.

[25] C. Li, M. Zhao, J. C. Li, Q. Jiang, *J. Appl. Phys.* **2008**, *104*, 113504.

[26] S. Singh, N. Wanderka, B. S. Murty, U. Glatzel, J. Banhart, *Acta Mater.* **2011**, *59*, 182.

[27] C. J. Tong, Y. L. Chen, S. K. Chen, J. W. Yeh, T. T. Shun, C. H. Tsau, S. J. Lin, S. Y. Chang, *Metall. Mater. Trans. A* **2005**, *36a*, 881.

[28] C. C. Tasan, Y. Deng, K. G. Pradeep, M. J. Yao, H. Springer, D. Raabe, *JOM.* **2014**, *66*, 1993.

[29] N. Park, I. Watanabe, D. Terada, Y. Yokoyama, P. K. Liaw, N. Tsuji, *Metall. Mater. Trans. A* **2014**, *46*, 1481.

[30] B. Schuh, F. Mendez-Martin, B. Volker, E. P. George, H. Clemens, R. Pippan, A. Hohenwarter, *Acta Mater.* **2015**, *96*, 258.

[31] F. Otto, A. Dlouhy, K. G. Pradeep, M. Kubenova, D. Raabe, G. Eggeler, E. P. George, *Acta Mater.* **2016**, *112*, 40.

[32] S. Singh, N. Wanderka, K. Kiefer, K. Siemensmeyer, J. Banhart, *Ultramicroscopy* **2011**, *111*, 619.

[33] Q. F. He, Z. Y. Ding, Y. F. Ye, Y. Yang, *JOM.* **2017**, *69*, 2092.

[34] Z. Wu, H. Bei, *Mater. Sci. Eng. A* **2015**, *640*, 217.

[35] H. M. Daoud, A. M. Manzoni, R. Völkl, N. Wanderka, U. Glatzel, *Adv. Eng. Mater.* **2015**, *17*, 1134.

[36] Y. Qiu, Y. J. Hu, A. Taylor, M. J. Styles, R. K. W. Marceau, A. V. Ceguerra, M. A. Gibson, Z. K. Liu, H. L. Fraser, N. Birbilis, *Acta Mater.* **2017**, *123*, 115.

[37] D. B. Miracle, J. D. Miller, O. N. Senkov, C. Woodward, M. D. Uchic, J. Tiley, *Entropy* **2014**, *16*, 494.

[38] S. J. Zhao, G. M. Stocks, Y. W. Zhang, *Acta Mater.* **2017**, *134*, 334.

[39] Y. Zhang, G. M. Stocks, K. Jin, C. Lu, H. Bei, B. C. Sales, L. Wang, L. K. Beland, R. E. Stoller, G. D. Samolyuk, M. Caro, A. Caro, W. J. Weber, *Nat Commun.* **2015**, *6*, 8736.

[40] C. Zhang, F. Zhang, K. Jin, H. B. Bei, S. L. Chen, W. S. Cao, J. Zhu, D. C. Lv, *J. Phase Equilib. Diffus.* **2017**, *38*, 434.

[41] J.-W. Yeh, *Annales de Chimie Science des Matériaux.* **2006**, *31*, 633.

[42] E. J. Pickering, N. G. Jones, *Int. Mater. Rev.* **2016**, *61*, 183.

[43] K. Y. Tsai, M. H. Tsai, J. W. Yeh, *Acta Mater.* **2013**, *61*, 4887.

[44] K. Kulkarni, G. P. S. Chauhan, *Aip Adv.* **2015**, 5.

[45] D. L. Beke, G. Erdelyi, *Mater. Lett.* **2016**, *164*, 111.

[46] J. Dąbrowa, W. Kucza, G. Cieślak, T. Kulik, M. Danielewski, J.-W. Yeh, *J. Alloys Compd.* **2016**, *674*, 455.

[47] M. Vaidya, S. Trubel, B. S. Murty, G. Wilde, S. V. Divinski, *J. Alloys Compd.* **2016**, *688*, 994.

[48] O. N. Senkov, S. V. Senkova, D. M. Dimiduk, C. Woodward, D. B. Miracle, *J. Mater. Sci.* **2012**, *47*, 6522.

[49] C. Huang, Y. Zhang, J. Shen, R. Vilar, *Surf. Coat. Technol.* **2011**, *206*, 1389.

[50] R. Sriharitha, B. S. Murty, R. S. Kottada, *J. Alloys Compd.* **2014**, *583*, 419.

[51] H. Zhang, Y.-Z. He, Y. Pan, S. Guo, *J. Alloys Compd.* **2014**, *600*, 210.

[52] C. Y. Cheng, J. W. Yeh, *Mater. Lett.* **2016**, *185*, 456.

[53] N. X. Zhou, T. Hu, J. J. Huang, J. Luo, *Scripta Mater.* **2016**, *124*, 160.

[54] B. Gorr, F. Mueller, H. J. Christ, T. Mueller, H. Chen, A. Kauffmann, M. Heilmaier, *J. Alloys Compd.* **2016**, *688*, 468.

[55] Y. Lu, Y. Dong, S. Guo, L. Jiang, H. Kang, T. Wang, B. Wen, Z. Wang, J. Jie, Z. Cao, H. Ruan, T. Li, *Sci Rep.* **2014**, *4*, 6200.

[56] S. C. Liang, D. C. Tsai, Z. C. Chang, T. N. Lin, M. H. Shiao, F. S. Shieu, *Electrochem. Solid State Lett.* **2012**, *15*, H5.

[57] B. Gludovatz, A. Hohenwarter, D. Catoor, E. H. Chang, E. P. George, R. O. Ritchie, *Science* **2014**, *345*, 1153.

[58] S.-Y. Chang, M.-K. Chen, D.-S. Chen, *J. Electrochem. Soc.* **2009**, *156*, G37.

[59] Y. H. Jo, S. Jung, W. M. Choi, S. S. Sohn, H. S. Kim, B. J. Lee, N. J. Kim, S. Lee, *Nat Commun.* **2017**, *8*, 15719.

[60] Y. F. Ye, Q. Wang, J. Lu, C. T. Liu, Y. Yang, *Mater. Today.* **2016**, *19*, 349.

[61] W. H. Wu, C. C. Yang, J. W. Yeh, *Annales De Chimie-Science Des Materiaux.* **2006**, *31*, 737.

[62] J. W. Yeh, Y. L. Chen, S. J. Lin, S. K. Chen, *Adv. Struct. Mater. Iii.* **2007**, *560*, 1.

[63] M. C. Gao, *JOM.* **2013**, *65*, 1749.

[64] M. H. Tsai, *Entropy* **2013**, *15*, 5338.

[65] B. Cantor, *Entropy* **2014**, *16*, 4749.

[66] S. Guo, *Mater. Sci. Technol.* **2015**, *31*, 1223.

[67] P. D. Jablonski, J. J. Licavoli, M. C. Gao, J. A. Hawk, *JOM.* **2015**, *67*, 2278.

[68] D. J. M. King, S. C. Middleburgh, A. G. McGregor, M. B. Cortie, *Acta Mater.* **2016**, *104*, 172.

[69] M. H. Chuang, M. H. Tsai, W. R. Wang, S. J. Lin, J. W. Yeh, *Acta Mater.* **2011**, *59*, 6308.

[70] M. A. Hemphill, T. Yuan, G. Y. Wang, J. W. Yeh, C. W. Tsai, A. Chuang, P. K. Liaw, *Acta Mater.* **2012**, *60*, 5723.

[71] H. Zhang, Y. Z. He, Y. Pan, *Scripta Mater.* **2013**, *69*, 342.

[72] M. J. Yao, K. G. Pradeep, C. C. Tasan, D. Raabe, *Scripta Mater.* **2014**, *72–73*, 5.

[73] C.-Y. Cheng, J.-W. Yeh, *Mater. Lett.* **2016**, *181*, 223.

[74] O. N. Senkov, G. B. Wilks, J. M. Scott, D. B. Miracle, *Intermetallics* **2011**, *19*, 698.

[75] P. K. Huang, J. W. Yeh, *Scripta Mater.* **2010**, *62*, 105.

[76] K. V. Yusenko, S. Riva, P. A. Carvalho, M. V. Yusenko, S. Arnaboldi, A. S. Sulthikh, M. Hanfland, S. A. Gromilov, *Scripta Mater.* **2017**, *138*, 22.

[77] L. C. Zhang, Z. Q. Shen, J. Xu, *J. Mater. Res.* **2011**, *18*, 2141.

[78] L. C. Zhang, K. B. Kim, P. Yu, W. Y. Zhang, U. Kunz, J. Eckert, *J. Alloys Compd.* **2007**, *428*, 157.

[79] L. C. Zhang, J. Xu, *J. Non-Cryst. Solids.* **2004**, *347*, 166.

[80] K. B. Kim, Y. Zhang, P. J. Warren, B. Cantor, *Philos. Mag.* **2003**, *83*, 2371.

[81] K. B. Kim, P. J. Warren, B. Cantor, *J. Non-Cryst. Solids.* **2003**, *317*, 17.

[82] L. Ma, L. Wang, T. Zhang, A. Inoue, *Mater. Trans.* **2002**, *43*, 277.

[83] J. Y. He, H. Wang, Y. Wu, X. J. Liu, T. G. Nieh, Z. P. Lu, *Mater. Sci. Eng. A* **2017**, *686*, 34.

[84] Z. Li, K. G. Pradeep, Y. Deng, D. Raabe, C. C. Tasan, *Nature* **2016**, *534*, 227.

[85] Z. M. Li, C. C. Tasan, K. G. Pradeep, D. Raabe, *Acta Mater.* **2017**, *131*, 323.

[86] Z. Li, D. Raabe, *Mater. Chem. Phys.* **2017**, 10.1016/j.matchemphys. 2017.04.050.

[87] J. Y. He, H. Wang, H. L. Huang, X. D. Xu, M. W. Chen, Y. Wu, X. J. Liu, T. G. Nieh, K. An, Z. P. Lu, *Acta Mater.* **2016**, *102*, 187.

[88] J. Y. He, H. Wang, Y. Wu, X. J. Liu, H. H. Mao, T. G. Nieh, Z. P. Lu, *Intermetallics* **2016**, *79*, 41.

[89] I. S. Wani, T. Bhattacharjee, S. Sheikh, Y. P. Lu, S. Chatterjee, P. P. Bhattacharjee, S. Guo, N. Tsuji, *Mater. Res. Lett.* **2016**, *4*, 174.

[90] I. S. Wani, T. Bhattacharjee, S. Sheikh, Y. Lu, S. Chatterjee, S. Guo, P. P. Bhattacharjee, N. Tsuji, *IOP Conf. Ser.: Mater. Sci. Eng.* **2017**, *194*, 012018.

[91] F. He, Z. Wang, P. Cheng, Q. Wang, J. Li, Y. Dang, J. Wang, C. T. Liu, *J. Alloys Compd.* **2016**, *656*, 284.

[92] D. G. Shaysultanov, G. A. Salishchev, Y. V. Ivanisenko, S. V. Zherebtsov, M. A. Tikhonovsky, N. D. Stepanov, *J. Alloys Compd.* **2017**, *705*, 756.

[93] B. Gwalani, V. Soni, M. Lee, S. A. Mantri, Y. Ren, R. Banerjee, *Mater. Des.* **2017**, *121*, 254.

[94] T. W. Zhang, Z. M. Jiao, Z. H. Wang, J. W. Qiao, *Scripta Mater.* **2017**, *136*, 15.

[95] L. Lu, M. L. Sui, K. Lu, *Science.* **2000**, *287*, 1463.

[96] Y. Wang, M. Chen, F. Zhou, E. Ma, *Nature.* **2002**, *419*, 912.

[97] H. Gleiter, *Prog. Mater Sci.* **1989**, *33*, 223.

[98] C. Suryanarayana, *Int. Mater. Rev.* **2013**, *40*, 41.

[99] V. Y. Gertsman, R. Birringer, *Scr. Metall. Mater.* **1994**, *30*, 577.

[100] M. Ames, J. Markmann, R. Karos, A. Michels, A. Tschope, R. Birringer, *Acta Mater.* **2008**, *56*, 4255.

[101] Y. Zou, J. M. Wheeler, H. Ma, P. Okle, R. Spolenak, *Nano Lett.* **2017**, *17*, 1569.

[102] S. Praveen, J. Basu, S. Kashyap, R. S. Kottada, *J. Alloys Compd.* **2016**, *662*, 361.

[103] A. H. Chokshi, *Mater. Chem. Phys.* **2017**, 10.1016/j.matchemphys. 2017.07.079.

[104] B. E. MacDonald, Z. Fu, B. Zheng, W. Chen, Y. Lin, F. Chen, L. Zhang, J. Ivanisenko, Y. Zhou, H. Hahn, E. J. Lavernia, *JOM.* **2017**, *69*, 2024.

[105] C. C. Koch, *J. Mater. Res.* **2017**, *32*, 3435.

[106] D. B. Miracle, *JOM.* **2017**, *69*, 2130.

[107] H. Y. Diao, R. Feng, K. A. Dahmen, P. K. Liaw, *Curr. Opin. Solid State Mater. Sci.* **2017**, *21*, 252.

[108] M. C. Gao, J.-W. Yeh, P. K. Liaw, Y. Zhang, *High-Entropy Alloys: Fundamentals and Applications*, Springer, Switzerland, **2016**.

[109] J. M. Wu, S. J. Lin, J. W. Yeh, S. K. Chen, Y. S. Huang, *Wear* **2006**, *261*, 513.

[110] T. K. Chen, M. S. Wong, *Thin Solid Films.* **2007**, *516*, 141.

[111] C. C. Tung, J. W. Yeh, T. T. Shun, S. K. Chen, Y. S. Huang, H. C. Chen, *Mater. Lett.* **2007**, *61*, 1.

[112] T. K. Chen, M. S. Wong, *Surf. Coat. Technol.* **2008**, *203*, 495.

[113] B. S. Li, Y. R. Wang, M. X. Ren, C. Yang, H. Z. Fu, *Mater. Sci. Eng. A* **2008**, *498*, 482.

[114] A. V. Kuznetsov, D. G. Shaisultanov, N. D. Stepanov, G. A. Salishchev, O. N. Senkov, *Mater. Sci. Forum.* **2012**, *735*, 146.

[115] D. G. Shaysultanov, N. D. Stepanov, A. V. Kuznetsov, G. A. Salishchev, O. N. Senkov, *JOM.* **2013**, *65*, 1815.

[116] S. Praveen, B. S. Murty, R. S. Kottada, *JOM.* **2013**, *65*, 1797.

[117] Y.-F. Kao, T.-J. Chen, S.-K. Chen, J.-W. Yeh, *J. Alloys Compd.* **2009**, *488*, 57.

[118] W. R. Wang, W. L. Wang, S. C. Wang, Y. C. Tsai, C. H. Lai, J. W. Yeh, *Intermetallics* **2012**, *26*, 44.

[119] Y. P. Wang, B. S. Li, M. X. Ren, C. Yang, H. Z. Fu, *Mater. Sci. Eng. A* **2008**, *491*, 154.

[120] F. J. Wang, Y. Zhang, *Mater. Sci. Eng. A* **2008**, *496*, 214.

[121] Y. J. Zhou, Y. Zhang, Y. L. Wang, G. L. Chen, *Appl. Phys. Lett.* **2007**, *90*, 181904.

[122] Y. J. Zhou, Y. Zhang, T. N. Kim, G. L. Chen, *Mater. Lett.* **2008**, *62*, 2673.

[123] J. W. Qiao, S. G. Ma, E. W. Huang, C. P. Chuang, P. K. Liaw, Y. Zhang, *Nano-Scale Amorphous Mater.* **2011**, *688*, 419.

[124] G. Laplanche, A. Kostka, O. M. Horst, G. Eggeler, E. P. George, *Acta Mater.* **2016**, *118*, 152.

[125] M. Laurent-Brocq, A. Akhatova, L. Perriere, S. Chebini, X. Sauvage, E. Leroy, Y. Champion, *Acta Mater.* **2015**, *88*, 355.

[126] K. V. S. Thurston, B. Gludovatz, A. Hohenwarter, G. Laplanche, E. P. George, R. O. Ritchie, *Intermetallics* **2017**, *88*, 65.

[127] D. Yim, M. J. Jang, J. W. Bae, J. Moon, C.-H. Lee, S.-J. Hong, S. I. Hong, H. S. Kim, *Mater. Chem. Phys.* **2017**, 10.1016/j. matchemphys.2017.06.013.

[128] J. W. Bae, J. Moon, M. J. Jang, D.-H. Ahn, S.-H. Joo, J. Jung, D. Yim, H. S. Kim, *Metall. Mater. Trans. A* **2017**, *48*, 4111.

[129] J. Moon, J. W. Bae, M. J. Jang, S. M. Baek, D. Yim, B.-J. Lee, H. S. Kim, *Mater. Chem. Phys.* **2017**, 10.1016/j.matchemphys. 2017.06.043.

[130] S. H. Joo, H. Kato, M. J. Jang, J. Moon, E. B. Kim, S. J. Hong, H. S. Kim, *J. Alloys Compd.* **2017**, *698*, 591.

[131] M. J. Jang, S.-H. Joo, C.-W. Tsai, J.-W. Yeh, H. S. Kim, *Met. Mater. Int.* **2016**, *22*, 982.

[132] E. J. Pickering, R. Munoz-Moreno, H. J. Stone, N. G. Jones, *Scripta Mater.* **2016**, *113*, 106.

[133] O. N. Senkov, C. F. Woodward, *Mater. Sci. Eng. A* **2011**, *529*, 311.

[134] O. N. Senkov, J. M. Scott, S. V. Senkova, F. Meisenkothen, D. B. Miracle, C. F. Woodward, *J. Mater. Sci.* **2012**, *47*, 4062.

[135] N. N. Guo, L. Wang, L. S. Luo, X. Z. Li, Y. Q. Su, J. J. Guo, H. Z. Fu, *Mater. Des.* **2015**, *81*, 87.

[136] C.-C. Juan, M.-H. Tsai, C.-W. Tsai, C.-M. Lin, W.-R. Wang, C.-C. Yang, S.-K. Chen, S.-J. Lin, J.-W. Yeh, *Intermetallics* **2015**, *62*, 76.

[137] N. N. Guo, L. Wang, L. S. Luo, X. Z. Li, R. R. Chen, Y. Q. Su, J. J. Guo, H. Z. Fu, *Mater. Sci. Eng. A.* **2016**, *651*, 698.

[138] C. C. Juan, M. H. Tsai, C. W. Tsai, W. L. Hsu, C. M. Lin, S. K. Chen, S. J. Lin, J. W. Yeh, *Mater. Lett.* **2016**, *184*, 200.

[139] M. Ogura, T. Fukushima, R. Zeller, P. H. Dederichs, *J. Alloys Compd.* **2017**, *715*, 454.

[140] J. C. Rao, H. Y. Diao, V. Ocelík, D. Vainchtein, C. Zhang, C. Kuo, Z. Tang, W. Guo, J. D. Poplawsky, Y. Zhou, P. K. Liaw, J. T. M. De Hosson, *Acta Mater.* **2017**, *131*, 206.

[141] C. Li, J. C. Li, M. Zhao, Q. Jiang, *J. Alloys Compd.* **2010**, *504*, S515.

[142] W. R. Wang, W. L. Wang, J. W. Yeh, *J. Alloys Compd.* **2014**, *589*, 143.

[143] D. M. King, S. C. Middleburgh, L. Edwards, G. R. Lumpkin, M. Cortie, *JOM.* **2015**, *67*, 2375.

[144] H. R. Sistla, J. W. Newkirk, F. Frank Liou, *Mater. Des.* **2015**, *81*, 113.

[145] S. Q. Xia, M. C. Gao, Y. Zhang, *Mater. Chem. Phys.* **2017**, 10.1016/j.matchemphys.2017.06.021.

[146] D. Y. Li, C. X. Li, T. Feng, Y. D. Zhang, G. Sha, J. J. Lewandowski, P. K. Liaw, Y. Zhang, *Acta Mater.* **2017**, *123*, 285.

[147] A. Munitz, S. Salhov, S. Hayun, N. Frage, *J. Alloys Compd.* **2016**, *683*, 221.

[148] W. H. Liu, Y. Wu, J. Y. He, Y. Zhang, C. T. Liu, Z. P. Lu, *JOM.* **2014**, *66*, 1973.

[149] T. M. Butler, M. L. Weaver, *J. Alloys Compd.* **2017**, *691*, 119.

[150] C. Zhang, F. Zhang, H. Y. Diao, M. C. Gao, Z. Tang, J. D. Poplawsky, P. K. Liaw, *Mater. Des.* **2016**, *109*, 425.

[151] F. He, Z. J. Wang, Q. F. Wu, J. J. Li, J. C. Wang, C. T. Liu, *Scripta Mater.* **2017**, *126*, 15.

[152] T. T. Shun, Y. C. Du, *J. Alloys Compd.* **2009**, *479*, 157.

[153] B. Gwalani, V. Soni, D. Choudhuri, M. Lee, J. Y. Hwang, S. J. Nam, H. Ryu, S. H. Hong, R. Banerjee, *Scripta Mater.* **2016**, *123*, 130.

[154] B. Gwalani, D. Choudhuri, V. Soni, Y. Ren, M. Styles, J. Y. Hwang, S. J. Nam, H. Ryu, S. H. Hong, R. Banerjee, *Acta Mater.* **2017**, *129*, 170.

[155] H. Y. Yasuda, H. Miyamoto, K. Cho, T. Nagase, *Mater. Lett.* **2017**, *199*, 120.

[156] I. S. Wani, G. D. Sathiaraj, M. Z. Ahmed, S. R. Reddy, P. P. Bhattacharjee, *Mater. Charact.* **2016**, *118*, 417.

[157] Q. H. Tang, Y. Huang, H. Cheng, X. Z. Liao, T. G. Langdon, P. Q. Dai, *Mater. Des.* **2016**, *105*, 381.

[158] T. T. Shun, Y. C. Du, *J. Alloys Compd.* **2009**, *478*, 269.

[159] T. T. Shun, C. H. Hung, C. F. Lee, *J. Alloys Compd.* **2010**, *495*, 55.

[160] Q. H. Tang, Y. Huang, Y. Y. Huang, X. Z. Liao, T. G. Langdon, P. Q. Dai, *Mater. Lett.* **2015**, *151*, 126.

[161] S. T. Chen, W. Y. Tang, Y. F. Kuo, S. Y. Chen, C. H. Tsau, T. T. Shun, J. W. Yeh, *Mater. Sci. Eng. A.* **2010**, *527*, 5818.

[162] L. C. Tsao, C. S. Chen, C. P. Chu, *Mater. Des.* **2012**, *36*, 854.

[163] M. H. Tsai, H. Yuan, G. M. Cheng, W. Z. Xu, W. W. W. Jian, M. H. Chuang, C. C. Juan, A. C. Yeh, S. J. Lin, Y. T. Zhu, *Intermetallics* **2013**, *33*, 81.

[164] C.-F. Lee, T.-T. Shun, *Metall. Mater. Trans. A* **2013**, *45*, 191.

[165] S. Z. Niu, H. C. Kou, T. Guo, Y. Zhang, J. Wang, J. S. Li, *Mater. Sci. Eng. A* **2016**, *671*, 82.

[166] Z. G. Wang, W. Zhou, L. M. Fu, J. F. Wang, R. C. Luo, X. C. Han, B. Chen, X. D. Wang, *Mater. Sci. Eng. A* **2017**, *696*, 503.

[167] T. F. Yang, Z. Tang, X. Xie, R. Carroll, G. Y. Wang, Y. G. Wang, K. A. Dahmen, P. K. Liaw, Y. W. Zhang, *Mater. Sci. Eng. A.* **2017**, *684*, 552.

[168] Y. Zhang, J. S. Li, J. Wang, S. H. Niu, H. C. Kou, *Metals* **2016**, *6*, 277.

[169] S. Y. Chen, X. Xie, B. L. Chen, J. W. Qiao, Y. Zhang, Y. Ren, K. A. Dahmen, P. K. Liaw, *JOM.* **2015**, *67*, 2314.

[170] C. Y. Hsu, C. C. Juan, W. R. Wang, T. S. Sheu, J. W. Yeh, S. K. Chen, *Mater. Sci. Eng. A* **2011**, *528*, 3581.

[171] S. Niu, H. Kou, Y. Zhang, J. Wang, J. Li, *Mater. Sci. Eng. A.* **2017**, *702*, 96.

[172] J. Antonaglia, X. Xie, Z. Tang, C. W. Tsai, J. W. Qiao, Y. Zhang, M. O. Laktionova, E. D. Tabachnikova, J. W. Yeh, O. N. Senkov, M. C. Gao, J. T. Uhl, P. K. Liaw, K. A. Dahmen, *JOM.* **2014**, *66*, 2002.

[173] H. Y. Yasuda, K. Shigeno, T. Nagase, *Scripta Mater.* **2015**, *108*, 80.

[174] S. Samal, M. R. Rahul, R. S. Kottada, G. Phanikumar, *Mater. Sci. Eng. A* **2016**, *664*, 227.

[175] N. D. Stepanov, D. G. Shaysultanov, M. S. Ozerov, S. V. Zherebtsov, G. A. Salishchev, *Mater. Lett.* **2016**, *185*, 1.

[176] S. H. Joo, H. Kato, M. J. Jang, J. Moon, C. W. Tsai, J. W. Yeh, H. S. Kim, *Mater. Sci. Eng. A* **2017**, *689*, 122.

[177] A. Gali, E. P. George, *Intermetallics* **2013**, *39*, 74.

[178] F. Otto, A. Dlouhy, C. Somsen, H. Bei, G. Eggeler, E. P. George, *Acta Mater.* **2013**, *61*, 5743.

[179] J. Moon, S. I. Hong, J. W. Bae, M. J. Jang, D. Yim, H. S. Kim, *Mater. Res. Lett.* **2017**, *5*, 472.

[180] M. J. Jang, D.-H. Ahn, J. Moon, J. W. Bae, D. Yim, J.-W. Yeh, Y. Estrin, H. S. Kim, *Mater. Res. Lett.* **2017**, *5*, 350.

[181] T. K. Liu, Z. Wu, A. D. Stoica, Q. Xie, W. Wu, Y. F. Gao, H. Bei, K. An, *Mater. Des.* **2017**, *131*, 419.

[182] Z. Wu, H. Bei, G. M. Pharr, E. P. George, *Acta Mater.* **2014**, *81*, 428.

[183] J. X. Fu, C. M. Cao, W. Tong, Y. X. Hao, L. M. Peng, *Mater. Sci. Eng. A* **2017**, *690*, 418.

[184] A. J. Zaddach, R. O. Scattergood, C. C. Koch, *Mater. Sci. Eng. A* **2015**, *636*, 373.

[185] N. D. Stepanov, D. G. Shaysultanov, R. S. Chernichenko, N. Y. Yurchenko, S. V. Zherebtsov, M. A. Tikhonovsky, G. A. Salishchev, *J. Alloys Compd.* **2017**, *693*, 394.

[186] J. W. Bae, J. Moon, M. J. Jang, D. Yim, D. Kim, S. Lee, H. S. Kim, *Mater. Sci. Eng. A* **2017**, *703*, 324.

[187] D. G. Shaysultanov, N. D. Stepanov, G. A. Salishchev, M. A. Tikhonovsky, *Phys. Met. Metallogr.* **2017**, *118*, 579.

[188] F. Zhang, Y. Wu, H. Lou, Z. Zeng, V. B. Prakapenka, E. Greenberg, Y. Ren, J. Yan, J. S. Okasinski, X. Liu, Y. Liu, Q. Zeng, Z. Lu, *Nat Commun.* **2017**, *8*, 15687.

[189] C. L. Tracy, S. Park, D. R. Rittman, S. J. Zinkle, H. Bei, M. Lang, R. C. Ewing, W. L. Mao, *Nat Commun.* **2017**, *8*, 15634.

[190] J. Moon, Y. Qi, E. Tabachnikova, Y. Estrin, W.-M. Choi, S.-H. Joo, B.-J. Lee, A. Podolskiy, M. Tikhonovsky, H. S. Kim, *Mater. Lett.* **2017**, *202*, 86.

[191] G. Bracq, M. Laurent-Brocq, L. Perriere, R. Pires, J. M. Joubert, I. Guillot, *Acta Mater.* **2017**, *128*, 327.

[192] G. D. Sathiaraj, M. Z. Ahmed, P. P. Bhattacharjee, *J. Alloys Compd.* **2016**, *664*, 109.

[193] G. Laplanche, P. Gadaud, O. Horst, F. Otto, G. Eggeler, E. P. George, *J. Alloys Compd.* **2015**, *623*, 348.

[194] J. Y. He, C. Zhu, D. Q. Zhou, W. H. Liu, T. G. Nieh, Z. P. Lu, *Intermetallics* **2014**, *55*, 9.

[195] P. P. Bhattacharjee, G. D. Sathiaraj, M. Zaid, J. R. Gatti, C. Lee, C. W. Tsai, J. W. Yeh, *J. Alloys Compd.* **2014**, *587*, 544.

[196] G. A. Salishchev, M. A. Tikhonovsky, D. G. Shaysultanov, N. D. Stepanov, A. V. Kuznetsov, I. V. Kolodiy, A. S. Tortika, O. N. Senkov, *J. Alloys Compd.* **2014**, *591*, 11.

[197] W. Zhou, L. M. Fu, P. Liu, X. D. Xu, B. Chen, G. Z. Zhu, X. D. Wang, A. D. Shan, M. W. Chen, *Intermetallics* **2017**, *85*, 90.

[198] N. Park, B.-J. Lee, N. Tsuji, *J. Alloys Compd.* **2017**, *719*, 189.

[199] V. Maier-Kiener, B. Schuh, E. P. George, H. Clemens, A. Hohenwarter, *Mater. Des.* **2017**, *115*, 479.

[200] D.-H. Lee, J.-A. Lee, Y. Zhao, Z. Lu, J.-Y. Suh, J.-Y. Kim, U. Ramamurty, M. Kawasaki, T. G. Langdon, J.-I. Jang, *Acta Mater.* **2017**, *140*, 443.

[201] G. D. Sathiaraj, P. P. Bhattacharjee, C. W. Tsai, J. W. Yeh, *Intermetallics* **2016**, *69*, 1.

[202] W. H. Liu, Y. Wu, J. Y. He, T. G. Nieh, Z. P. Lu, *Scripta Mater.* **2013**, *68*, 526.

[203] D. Wu, J. Zhang, J. C. Huang, H. Bei, T. G. Nieh, *Scripta Materialia*. **2013**, *68*, 118.

[204] F. Otto, N. L. Hanold, E. P. George, *Intermetallics* **2014**, *54*, 39.

[205] S. I. Hong, J. Moon, S. K. Hong, H. S. Kim, *Mater. Sci. Eng. A* **2017**, *682*, 569.

[206] W. Woo, E. W. Huang, J.-W. Yeh, H. Choo, C. Lee, S.-Y. Tu, *Intermetallics* **2015**, *62*, 1.

[207] S. R. Reddy, S. Bapari, P. P. Bhattacharjee, A. H. Chokshi, *Mater. Res. Lett.* **2017**, *5*, 408.

[208] R. R. Eleti, T. Bhattacharjee, L. Zhao, P. P. Bhattacharjee, N. Tsuji, *Mater. Chem. Phys.* **2017**, 10.1016/j.matchemphys.2017.06.062.

[209] O. N. Senkov, G. B. Wilks, D. B. Miracle, C. P. Chuang, P. K. Liaw, *Intermetallics* **2010**, *18*, 1758.

[210] O. N. Senkov, J. M. Scott, S. V. Senkova, D. B. Miracle, C. F. Woodward, *J. Alloys Compd.* **2011**, *509*, 6043.

[211] O. N. Senkov, S. V. Senkova, C. Woodward, *Acta Mater.* **2014**, *68*, 214.

[212] Y. Liu, Y. Zhang, H. Zhang, N. J. Wang, X. Chen, H. W. Zhang, Y. X. Li, *J. Alloys Compd.* **2017**, *694*, 869.

[213] B. Gorr, M. Azim, H. J. Christ, T. Mueller, D. Schliephake, M. Heilmaier, *J. Alloys Compd.* **2015**, *624*, 270.

[214] C. M. Liu, H. M. Wang, S. Q. Zhang, H. B. Tang, A. L. Zhang, *J. Alloys Compd.* **2014**, *583*, 162.

[215] S. Mohanty, N. P. Gurao, P. Padaikathan, K. Biswas, *Mater. Charact.* **2017**, *129*, 127.

[216] J. W. Wang, Y. Liu, B. Liu, Y. Wang, Y. K. Cao, T. C. Li, R. Zhou, *Mater. Sci. Eng. A* **2017**, *689*, 233.

[217] N. D. Stepanov, D. G. Shaysultanov, N. Y. Yurchenko, S. V. Zherebtsov, A. N. Ladygin, G. A. Salishchev, M. A. Tikhonovsky, *Mater. Sci. Eng. A* **2015**, *636*, 188.

[218] N. Nayan, G. Singh, S. V. S. N. Murty, A. K. Jha, B. Pant, K. M. George, U. Ramamurty, *Intermetallics* **2014**, *55*, 145.

[219] C. H. Tsau, *Mater. Sci. Eng. A* **2009**, *501*, 81.

[220] X. Xian, Z. Zhong, B. Zhang, K. Song, C. Chen, S. Wang, J. Cheng, Y. Wu, *Mater. Des.* **2017**, *121*, 229.

[221] A. M. Manzoni, S. Singh, H. M. Daoud, R. Popp, R. Volkl, U. Glatzel, N. Wanderka, *Entropy* **2016**, *18*, 104.

[222] P. Sathiyamoorthi, J. Basu, S. Kashyap, K. G. Pradeep, R. S. Kottada, *Mater. Des.* **2017**, *134*, 426.

[223] T. K. Tsao, A. C. Yeh, C. M. Kuo, H. Murakami, *Entropy* **2016**, *18*.

[224] O. N. Dogan, B. C. Nielsen, J. A. Hawk, *Oxid. Met.* **2013**, *80*, 177.

[225] T. M. Butler, J. P. Alfano, R. L. Martens, M. L. Weaver, *JOM.* **2014**, *67*, 246.

[226] J. C. Jiang, X. Y. Luo, *Adv. Technol. Mater. Mater. Process, Pts 1–3.* **2013**, *652–654*, 1115.

[227] W. Kai, C. C. Li, F. P. Cheng, K. P. Chu, R. T. Huang, L. W. Tsay, J. J. Kai, *Corros. Sci.* **2017**, *121*, 116.

[228] J. Dąbrowa, G. Cieślak, M. Stygar, K. Mroczka, K. Berent, T. Kulik, M. Danielewski, *Intermetallics* **2017**, *84*, 52.

[229] G. Laplanche, U. F. Volkert, G. Eggeler, E. P. George, *Oxid. Met.* **2016**, *85*, 629.

[230] W. Kai, C. C. Li, F. P. Cheng, K. P. Chu, R. T. Huang, L. W. Tsay, J. J. Kai, *Corros. Sci.* **2016**, *108*, 209.

[231] G. R. Holcomb, J. Tylczak, C. Carney, *JOM.* **2015**, *67*, 2326.

[232] W. Kai, W. L. Jang, R. T. Huang, C. C. Lee, H. H. Hsieh, C. F. Du, *Oxid. Met.* **2005**, *63*, 169.

[233] Z. Rao, X. Wang, Q. Wang, T. Liu, X. Chen, L. Wang, X. Hui, *Adv. Eng. Mater.* **2017**, *19*.

[234] X. Chen, Y. W. Sui, J. Q. Qi, Y. Z. He, F. X. Wei, Q. K. Meng, Z. Sun, *J. Mater. Res.* **2017**, *32*, 2109.

[235] W.-L. Hsu, H. Murakami, J.-W. Yeh, A.-C. Yeh, K. Shimoda, *J. Electrochem. Soc.* **2016**, *163*, C752.

[236] W.-L. Hsu, Y.-C. Yang, C.-Y. Chen, J.-W. Yeh, *Intermetallics* **2017**, *89*, 105.

[237] Z. B. Cai, X. F. Cui, G. Jin, Z. Liu, W. Zheng, Y. Li, L. Q. Wang, *Met. Mater. Int.* **2017**, *23*, 1012.

[238] V. Dolique, A. L. Thomann, P. Brault, Y. Tessier, P. Gillon, *Surf. Coat. Technol.* **2010**, *204*, 1989.

[239] C.-Y. Cheng, J.-W. Yeh, *Mater. Lett.* **2016**, *185*, 456.

[240] X. Feng, J. Zhang, Z. Xia, W. Fu, K. Wu, G. Liu, J. Sun, *Mater. Lett.* **2018**, *210*, 84.

[241] M.-H. Tsai, J.-W. Yeh, J.-Y. Gan, *Thin Solid Films.* **2008**, *516*, 5527.

[242] M.-H. Tsai, C.-W. Wang, C.-W. Tsai, W.-J. Shen, J.-W. Yeh, J.-Y. Gan, W.-W. Wu, *J. Electrochem. Soc.* **2011**, 158.

[243] M.-H. Tsai, C.-W. Wang, C.-H. Lai, J.-W. Yeh, J.-Y. Gan, *Appl. Phys. Lett.* **2008**, 92.

[244] Z. J. Wang, S. Guo, Q. Wang, Z. Y. Liu, J. C. Wang, Y. Yang, C. T. Liu, *Intermetallics* **2014**, *53*, 183.

[245] D. H. Lee, M. Y. Seok, Y. Zhao, I. C. Choi, J. He, Z. P. Lu, J. Y. Suh, U. Ramamurty, M. Kawasaki, T. G. Langdon, J. I. Jang, *Acta Mater.* **2016**, *109*, 314.

[246] S.-Y. Chang, S.-Y. Lin, Y.-C. Huang, C.-L. Wu, *Surf. Coat. Technol.* **2010**, *204*, 3307.